Los Alamos Environmental Restoration Records Processing Facility

ER Record I.D.# 70012

LOS ALAMOS NATIONAL LABORATORY
ENVIRONMENTAL RESTORATION
Records Processing Facility
ER Records Index Form

ER ID NO. 70012 *Date Received:* 5/17/01 *Processor:* DSV *Page Count:* 55

Privileged: (Y/N) N *Record Category:* P

FileFolder: N/A

Correction: (Y/N) N *Corrected No.* 0 *Corrected By Number:* 0

Administrative Record: (Y/N) Y

Refilmed: (Y/N) N *Old ER ID Number:* 0 *New ER ID Number:* 0

Miscellaneous Comments:

N/A

14240

THIS FORM IS SUBJECT TO CHANGE. CONTACT THE RPF FOR LATEST VERSION. (JUNE 1997)

#70012

55

LA-UR-95-2735

Numerical Modeling of Unsaturated Groundwater Flow and Radionuclide Transport at MDA G

Kay H. Birdsell, EES-5
Wendy E. Soll, EES-5
Nina D. Rosenberg, EES-5
Bruce A. Robinson, EES-5

September 1995

MAY 17 2005

NUMERICAL MODELING of UNSATURATED GROUNDWATER FLOW and RADIONUCLIDE TRANSPORT at MDA G

by

Kay Birdsell, Wendy Soll,
Nina Rosenberg and Bruce Robinson

ABSTRACT

This report presents a post-disposal groundwater flow model and radionuclide transport calculations for Material Disposal Area (MDA) G located on Mesita del Buey at Los Alamos National Laboratory. We first present a pre-disposal flow model based on comparisons of calculated saturations for a range of infiltration rates to in-situ data measured at or near the site. Results from this study suggest that net infiltration rates into the mesa surface must be extremely low, about 0.001 cm/yr, to match site data for the mesa-top units. However, a net infiltration rate of 1 mm/yr is required to match saturations in the deeper units. This suggests that perhaps an additional source of water supplies water to the deeper units. Since results from separate fracture flow studies of Bandelier Tuff suggest that episodic fracture flow occurs only under extremely wet conditions and also preliminary calculations suggest that transient events are damped near the surface, we use a steady-state continuum approach in our post-disposal flow model. In this model, an infiltration rate of 1 mm/yr is applied over the undisturbed surface of the mesa top with a higher infiltration rate, 4 mm/yr, applied to the five disposal pits in the modeled cross-section of the site. This post-disposal flow model forms the basis for radionuclide transport calculations. We also investigate the importance of evaporation from mesa sides and fractures on flow within the mesa and conclude that it very likely plays a key role in keeping the mesa dry. However, this process was not explicitly included as part of the post-disposal model.

Transport of 30 parent radionuclides from the historical inventory at MDA G is considered in this report. Based on these transport calculations, the following parent radionuclides are considered to be the most important to the Performance Assessment (PA) of MDA G: Am-241, C-14, Pu-241, and Np-237. These species reach their peak concentrations before 10,000 yrs. Np-237 is transported more quickly than most species because of its very low Kd (0.007) which leads to a peak concentration at 4500 yrs. Since Am-241 and Pu-241 both decay rather quickly to Np-237, these radionuclides are also important. C-14 is potentially important because it does not sorb, and peaks at about 3,900 yrs. Transport calculation were not performed for the following radionuclides because their half-lives are short compared to there transport rates: Ag-108m, Ba-133, Cd-113m, Co-60, Cs-137, Eu-152, Eu-154, Gd-148, H-3, Sm-151, Sr-90, Nb-94, and Ra-226. Transport calculations performed for the following radionuclides showed that they reach peak concentrations at times larger than 10,000 yrs: Hf-182, Mo-93, Pu-238, Pu-239, Pu-240, Pu-242, Tc-99, Th-232, U-233, U-234, U-235, U-236, and U-238. Concentration breakthrough curves are presented for use as input to a dose assessment model for the Area G PA.

The main uncertainty in the calculations stems from uncertainties concerning the hydrologic processes that control flow at the site. Specifically, the roles of evaporation, transient infiltration, and fracture flow are still not clear. The main data uncertainties are in the hydrologic properties for the bottom 70% of the vadose zone at the site and in site-specific sorption coefficients (Kd) for weakly sorbing radionuclides. Our calculations take no credit for transport through this lower portion of the vadose zone, which is an extremely conservative assumption.

ABSTRACT i

List of Figures and Tables iii

INTRODUCTION 1

PART I - PRE-DISPOSAL FLOW MODEL 3
- Modeling Approach 3
- Pre-disposal Flow Modeling Results 6
- Effect of Infiltration from Canyon Bottoms 8
- Response Time to Changes in Surface Infiltration 10
- Sensitivity to Saturated Hydraulic Conductivity 10

PART II - A STUDY OF SPECIFIC FLOW PROCESSES 12
- Fracture Flow 12
- Evaporation from Mesa Sides, Fractures, and Surge Beds 14

PART III - POST-DISPOSAL FLOW MODEL 19
- Summary of Findings From Part I and Part II 19
- Effect of Disposal Pits 19
- Resulting Flow Model 19

PART IV - TRANSPORT MODELING 22
- Modeling Approach 22
- Generic Source Term 22
- Historic Inventory 24
  - Screening 25
  - Results of Transport Calculations 26
    - Am-241 28
    - C-14 29
    - Hf-182 30
    - Np-237 31
    - Pu-238 32
    - Pu-239 33
    - Pu-240 34
    - Pu-241 35
    - Pu-242 36
    - Tc-99 37
    - Th-232 38
    - U-233 39
    - U-234 40
    - U-235 41
    - U-236 42
    - U-238 43

SUMMARY OF RESULTS 44

DISCUSSION OF UNCERTAINTY 46

REFERENCES 48

FIGURES

Figure 1. Cross section of Western MDA G (based on Krier et al, 1995) used for 2-dimensional simulations..... 4

Figure 2. Computational Grid for MDA G flow and transport modeling..... 5

Figure 3. Comparison of site data (gray boxes) to calculated steady-state saturation profiles for several infiltration rates..... 6

Figure 4. Two-dimensional saturation profile for the pre-disposal flow model, calculated with an infiltration rate of 1 mm/yr..... 7

Figure 5. Saturation Profiles for Infiltration at 1 mm/yr with a) No-flow boundaries along canyons, and b) Canyon saturations fixed at 0.9 in Pajarito Canyon and 0.5 in Canada del Buey..... 9

Figure 6. Comparison of site data (gray boxes) to calculated steady-state saturation profiles for several variations in K_{sat}. The infiltration rate is 0.01 cm/yr..... 11

Figure 7. System Configuration for Fracture Flow Study..... 12

Figure 8. Problem set up for study of evaporative effects from mesa sides and from fractures..... 14

Figure 9. Resulting Saturation Profiles for Evaporation along a Mesa Edge (right side) and from fractures with 5-m and 10-m spacing, Unit 2b..... 15

Figure 10. Resulting Saturation Profiles for Evaporation along a Mesa Edge (right side) and from fractures with 5-m and 10-m spacing, Unit 2a..... 16

Figure 11. Resulting saturation profile for evaporation along the "surge beds" at the Unit 2b/2a interface compared to that for infiltration alone..... 17

Figure 12. Resulting capillary pressure profile for evaporation along the "surge beds" at the Unit 2b/2a interface compared infiltration alone and to data from Rogers et al. (1995) for Borehole G-5..... 17

Figure 13. Two-dimensional cross section used for numerical simulations, modified to indicate five waste disposal pits..... 20

Figure 14.	Saturation Profile for the Steady-State, Post-Disposal Flow Model of MDA G	21
Figure 15.	(a) Time dependent, generic source term and (b) Concentration breakthrough curve for generic source term assuming different Kd values	23
Figure 16.	(a) Source term and (b) Concentration breakthrough curve for Am-241	28
Figure 17.	(a) Source term and (b) Concentration breakthrough curve for C-14	29
Figure 18.	(a) Source term and (b) Concentration breakthrough curve for Hf-182.	30
Figure 19.	(a) Source term and (b) Concentration breakthrough curve for Np-237	31
Figure 20.	(a) Source term and (b) Concentration breakthrough curve for Pu-238.	32
Figure 21.	(a) Source term and (b) Concentration breakthrough curve for Pu-239.	33
Figure 22.	(a) Source term and (b) Concentration breakthrough curve for Pu-240.	34
Figure 23.	(a) Source term and (b) Concentration breakthrough curve for Pu-241.	35
Figure 24.	(a) Source term and (b) Concentration breakthrough curve for Pu-242.	36
Figure 25.	(a) Source term and (b) Concentration breakthrough curve for Tc-99.	37
Figure 26.	(a) Source term and (b) Concentration breakthrough curve for Th-232	38
Figure 27.	(a) Source term and (b) Concentration breakthrough curve for U-233.	39
Figure 28.	(a) Source term and (b) Concentration breakthrough curve for U-234	40
Figure 29.	(a) Source term and (b) Concentration breakthrough curve for U-235	41
Figure 30.	(a) Source term and (b) Concentration breakthrough curve for U-236	42

Figure 31. (a) Source term and (b) Concentration breakthrough curve for U-238 43

TABLES

Table 1. Mean Hydrologic Properties..... 3

Table 2. Times to peak concentration and first arrival as a function of Kd for the generic source term..... 24

Table 3. Estimated times to peak concentration and first arrival as a function of Kd for the generic source term..... 24

Table 4. Screening criteria for radionuclides..... 25

Table 5. Half-lives and Sorption Coefficients required for transport simulations..... 26

Table 6. Peak Arrival Times for Nuclides requiring Full Transport Calculations..... 44

INTRODUCTION

Transport calculations are performed to predict the long-term migration rates of water soluble radionuclides at MDA G in support of a radiological performance assessment (PA) for the site (Hollis et al., 1995). We are examining the flow behavior at the site in order to subsequently make predictions of radionuclide migration from the site toward the accessible environment. This report has four main sections which investigate and describe the flow and transport at MDA G through modeling studies. In Part I, we describe a steady-state flow model for a two-dimensional cross section at the area under predisposal conditions. In Part II, we take a closer look at some processes, namely fracture flow and evaporation from mesa sides, fractures, and surge beds, to better understand how these processes may affect flow at the site. In Part III, we use the information from Parts I and II to develop a steady flow model for MDA G under current or post-disposal conditions. This is the model that is used for the subsequent PA transport calculations presented in Part IV.

The conceptual model of subsurface transport beneath MDA G (Turin, 1995) describes the flow and transport mechanisms at the site as alternating between an episodic infiltration state and the normal drying state. The fracture system may allow episodic deep infiltration during spring snow melt or summer thunderstorms. Such infiltration events are then followed by the more typical process of evaporative drying at the mesa surface and in the fracture system. Leakage from the alluvial aquifer in Pajarito Canyon may act as active recharge to the deep aquifer and provide a faster flow path for radionuclides migrating downward from the site if water from the canyons flow laterally beneath the mesa.

In Part I, the predisposal or background flow model, we consider steady infiltration through and beneath the mesa under predisposal conditions using a two-dimensional representation of MDA G. Simulated results are compared to measured saturation data from the site. We look at the sensitivity of the system to infiltration from wet canyon bottoms, uncertainties in hydraulic conductivity, and short-term deviations from the steady infiltration rate.

In Part II, we study some of the processes that complicate the flow in this region, as pointed out in the site conceptual model (Turin, 1995). These processes are fracture flow and evaporation from the mesa sides, fractures and surge beds. The mesas on which LANL sits are highly fractured, with observed fracture spacings of 2-3 meters (Krier et al., 1995). Mapping of the regional fractures has identified areas where the fractures are filled and where clay and caliche coatings exist along some of the fracture walls. Continuity of fractures from the upper units of the mesas to lower units is unknown. The ubiquitousness of the fractures, and the potential for fractures to act both as a fast path for water or contaminants during episodic infiltration events and as conduits for evaporation under dry conditions confirm the need to understand the role that fractures play in this system. For this reason, we have undertaken a study to analyze the influence of different fracture characteristics, namely fracture coatings and fills, on the imbibition of water from fractures during infiltration events. We have also looked at the role that fractures may play in evaporation at the site. These processes are transient and occur local to the fracture making them more difficult to study at the mesa scale. For this reason, this modeling is done over smaller spatial and temporal scales.

In Part III, we summarize the lessons learned from Parts I and II, make some assumptions regarding the effect that the disposal pits have on flow at the site, and combine this information into a post-disposal flow model that is used for calculating transport of radionuclides from the pits. This flow model is closely tied to the background flow model and assumes steady infiltration.

Finally in Part IV, we perform transport calculations for radionuclides that are present in the historic inventory at MDA G. A time dependent source term is used to describe the release of the nuclides from the disposal units. We use a generic source term to develop a screening tool that predicts breakthrough as a function of sorption coefficient. This screening tool is used to eliminate many nuclides from further consideration. Results for transport simulations for the remaining nuclides are presented.

Our approach here is to study flow and transport at MDA G using a steady flow assumption. The calculations are performed with the finite element code FEHM (Zyvoloski et al., 1995) which simulates fluid flow, heat transport, and contaminant transport through porous and fractured media. Steady infiltration is assumed in previous PA calculations used for other sites (Barnard and Dockery, 1991, and Wood et al., 1994). The basis behind the steady flow model is that although processes at a site are clearly transient, that at depth and over long time scales, they average out to yield a near steady flow. By using a high, steady infiltration rate and other conservative assumptions concerning flow at the site, the subsequent transport calculations are then also *assumed to be* conservative.

The steady flow model should be questioned at each site, and it clearly conflicts with the site conceptual model for MDA G. However, it is the obvious first step for predicting long-term flow and transport at any site. The next step is to study the system in a transient fashion. FEHM has the capability to study transient matrix/fracture flow and transport using a dual permeability model. The dual permeability model is currently being verified, and we hope to use it in the future to challenge the steady flow and transport model. Calculations would study the system response to episodic infiltration events followed by drying in the fracture system over time periods which are shorter than a typical performance assessment calculation (hundreds rather than tens-of-thousands of years) because of numerical constraints. The value of such calculations would be to determine the applicability and the conservatism of the steady flow model by helping to determine whether contaminant transport is significantly enhanced by periodic pulsing of the fracture system.

PART I - PRE-DISPOSAL FLOW MODEL

Modeling Approach

Our approach for modeling the flow behavior at MDA G is to first run a set of background steady flow simulations and to compare the results to site field data. The computational grid is based on realistic stratigraphy and topography. We use a two-dimensional cross section defined by Krier (Krier et al., 1995) as shown in Figure 1. The topographic information was obtained for this cross section from contour data developed from the LANL Environmental Restoration Project aerial survey, performed in September, 1991. We assume that uniform, steady infiltration occurs along the mesa top. Several infiltration rates are applied: 1.0 cm/yr, 0.1 cm/yr, 0.01 cm/yr, 0.001 cm/yr and 0.0 cm/yr. Infiltration is applied uniformly over the top of the mesa from 850 ft (259 m) to 1750 ft (533 m) along the distance of the cross section, as shown in Figure 1. Evaporation and runoff from the mesa top are indirectly accounted for in the assumed low infiltration rates which are much lower than the average precipitation rate measured at MDA G, 35.6 cm/yr (Bowen, 1990). Figure 2 shows the computational grid used for the flow and transport simulations for this cross section. The grid has 2,931 nodes and is made up of 5,581 triangular elements. It extends to the water table.

Mean hydrologic properties (Krier et. al, 1995) are assigned to Unit 2b, Unit 2a, Unit 1b, Unit 1a, the Cerro Toledo, and the Otowi Member. These properties are shown in Table 1. Properties for the Otowi Member are assigned to the Guaje Pumice, the Cerros del Rio basalts, and the Puye Formation because no hydrologic parameters are available for these units. Samples collected thus far for the basalts display extreme variability (Turin, 1995) so that no best guess for hydrologic properties can be made. Because of the lack of data, radionuclide transport times through the lower three units (the Guaje Pumice, the Cerros del Rio basalts, and the Puye Formation) will be neglected. We assume that assigning hydrologic properties of the Otowi Member to these three units for the purpose of establishing a flow field will have little effect on the subsequent transport calculations. For these simulations, the side boundaries are impermeable. The bottom boundary is held at a saturation equal to 0.99 to represent a water table boundary condition.

****

Table 1. Mean Hydrologic Properties (from Krier et. al, 1995)

Unit	Ksat (cm/s)	porosity	van Genuchten param (θ_r, α (cm^{-1}), n)
Unit 2b	4.27×10^{-4}	0.481	0.013, 0.0060, 1.890
Unit 2a	1.48×10^{-4}	0.517	0.002, 0.0030, 1.932
Unit 1b	1.67×10^{-4}	0.509	0.009 0.0033,1.647
Unit 1a	1.88×10^{-4}	0.480	0.006, 0.0053, 1.745
Cerro Toledo	8.65×10^{-4}	0.473	0.008, 0.0152, 1.506
Otowi Member	2.49×10^{-4}	0.435	0.0188, 0.0059, 1.713
Guaje Pumice	*	*	*
Cerros del Rio basalts	*	*	*
Puye Formation	*	*	*

* Data is unavailable. Properties for Otowi Member used for these units.

****

Within the background flow study, we consider the effect that infiltration from canyon bottoms has on the flow system. Increased saturations are applied as boundary conditions (see Figure 1) to the adjacent canyons. We also look at the system response time to deviations from the steady infiltration rate, and consider the sensitivity of the resulting saturation profiles to the saturated hydraulic conductivity of the various stratigraphic units.

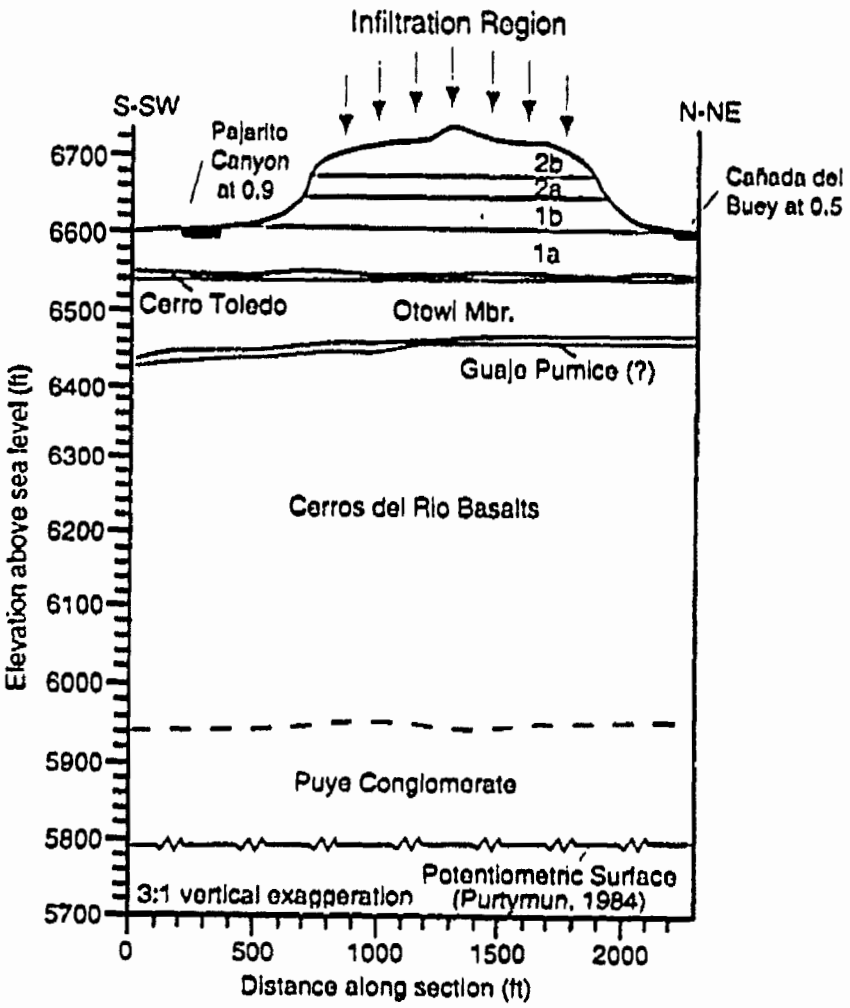

Figure 1. Cross section of Western MDA G (based on Krier et al, 1995) used for 2-dimensional simulations. Boundary conditions for infiltration region and fixed canyon saturations are indicated.

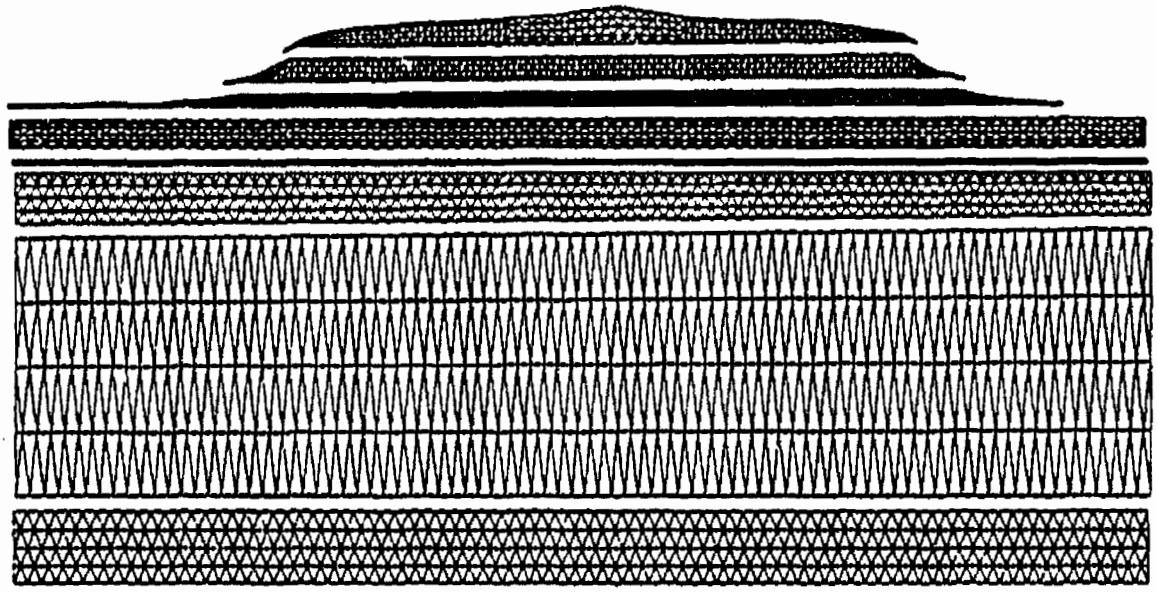

Figure 2. Computational Grid for MDA G flow and transport modeling. Strata include (top to bottom) Unit 2b, Unit 2a, Unit 1b, Unit 1a, Cerro Toledo, Otowi Member, Cerros del Rio Basalts, and Puye Conglomerate.

Pre-disposal Flow Modeling Results

Figure 3 shows steady-state saturation profiles at the center of the mesa for the 5 infiltration rates. The measured in-situ saturation data are also shown. The simulations were run for a period of 500,000 years to achieve steady flow throughout the domain at each flow rate. The simulation results are compared to saturation data from Unit 2b down through the Otowi Member. Here we see that the shape of the curves mimic the shape of the data (e.g. saturations decrease from Unit 2b to Unit 2a and then increase again in Unit 1b, etc.). However, no single infiltration rate fits through the entire set of saturation data. Results for the lowest infiltration rates (0.001 and 0.0 cm/yr) most closely match the site saturation data in Units 2b and 2a, the two units located within the mesa top. Higher infiltration rates (0.1 and 0.01 cm/yr) are needed to match the saturation data from Units 1b and 1a, and an even higher rate (~1 cm/yr) is needed to match the data in the Cerro Toledo and Otowi Member. Figure 4 shows the full 2-d saturation profile for the mesa calculated with an infiltration rate of 0.1 cm/yr. The saturation at the edges of the mesa is lower because infiltration occurs only along the mesa top as shown in Figure 1. Water added at the top spreads laterally to the drier sides but can not leave the system through the sides of the mesa which are impermeable to water flow in these particular simulations.

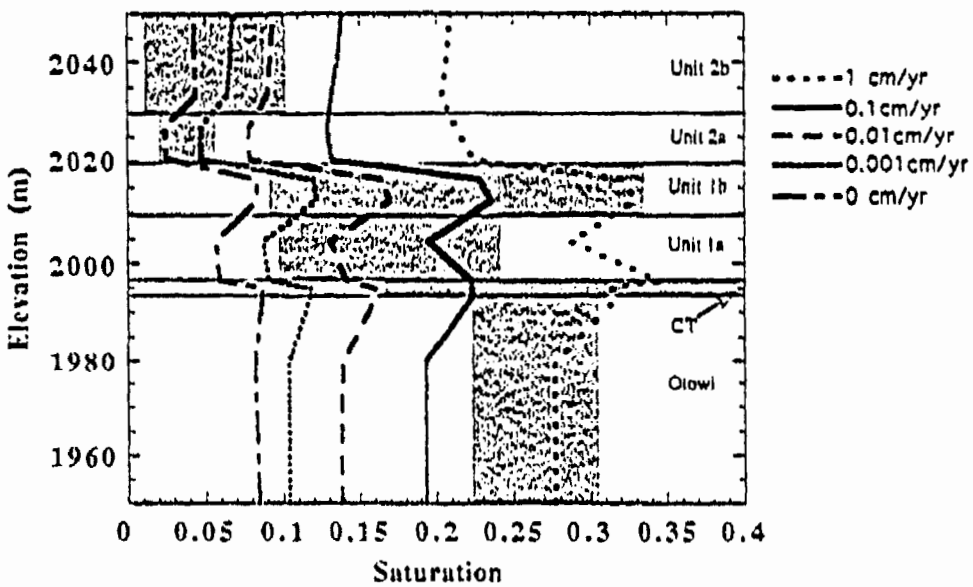

Figure 3. Comparison of site data (gray boxes) to calculated steady-state saturation profiles for several infiltration rates. Calculated profiles are located at the center of the cross section.

The steady saturation profile calculated for any single infiltration rate does not match all the in-situ saturation data gathered at the site. Saturations within the mesa top (Units 2b and 2a) are extremely dry. Saturations below the base of the mesa (Unit 1b and below) are higher. Several factors which may contribute to this discrepancy include: 1) infiltration from canyons resulting in higher saturations below the base of the mesa, 2) evaporation from the mesa sides and from fractures resulting in very low saturations within the mesa top, 3) uncertainty and heterogeneity in

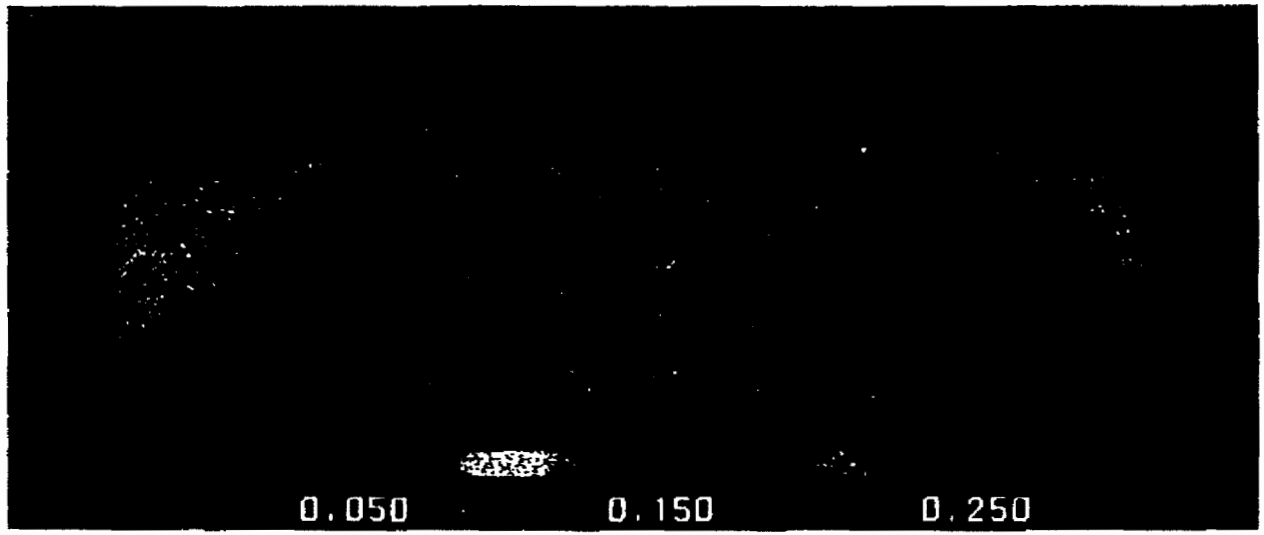

Figure 4 Two dimensional saturation profile for the pre disposal flow model, calculated with an infiltration rate of 1 mm/yr

UNCLASSIFIED - NON-PROPRIETARY

hydrologic properties yielding different calculated saturation profiles, 4) unsteady infiltration rates, and 5) fracture flow resulting in increased moisture in deeper units. In the remainder of the flow modeling sections of this report, we look at the effects that these various factors may have on the steady state saturation profiles described here.

Effect of Infiltration from Canyon Bottoms

A perennial aquifer exists in Pajarito Canyon while an intermittent stream runs through Canada del Buey (Turin, 1995). Infiltration from these two canyons which bound MDA G may flow laterally causing increased flow rates beneath the mesa. Such a source could decrease contaminant transport times and contribute to the higher saturations measured beneath the canyon floors relative to the mesa top. Simulations are used to study the effects that moisture from the canyons may have on the flow system beneath the mesa.

We use the computational grid for the DE cross section (Fig. 2) for the canyon study. Fixed saturations are assigned to nodes that represent the canyon floors (Fig. 1). A saturation value of 0.9 was chosen for Pajarito Canyon to represent the perennial aquiver, and a value of 0.5 was chosen for Canada del Buey as the intermittent stream. These simulations are run to steady state with a constant infiltration rate along the mesa top of 0.1 cm/yr. Saturation distributions as well as a particle tracking technique are used to study the flow field. Figure 5 shows color figures of the saturation distribution for the entire grid with (Fig. 5b) and without (Fig. 5a) the wet canyons. (Note that Fig. 5a represents the same information as Fig. 4, but the color scale is changed.) The increased moisture clearly increases saturations in the area below the canyons themselves, but has a weaker effect beneath the mesa. The saturation profile calculated for the center of the grid matches that for the simulation with the same infiltration rate but nonflowing boundaries along the canyons. This indicates that saturations and velocities are not affected by the wet canyons at the center of the grid. However, faster contaminant transport near the outer edges of the mesa might still occur.

To determine whether increased transport occurs near the canyons, a line of tracer particles was placed at the base of Unit 2a. Time snap-shots were studied to see the difference in particle movement between the simulations with and without the wet canyons. The difference is quite small over a 10,000 yr simulation. Particles located near the outer edges at the base of the mesa are pushed a few meters in toward the center by water flow from the canyon. However, these particles are nearly stagnant. The majority of the particles, which travel with water infiltrating from the mesa top, feel no influence from the wetter canyons.

These preliminary simulations indicate that waste traveling from MDA G should experience very little decrease in travel times due to infiltration from the adjacent wetter canyons. There are, however, several details not included in these simulations which could change these results. First, only small portions of the canyons floors are treated as regions of constant saturation in these simulations (see Figure 1). A more appropriate boundary condition may be to apply infiltration over larger portions of the canyon floors, similar to the boundary condition used on the mesa top. This would represent infiltration of run-off and might yield more wide-spread higher saturations in the units from Unit 1a downward. Also, these simulations use isotropic, porous media representations for the units that underlie the canyons. Although few fractures are observed in these units (Krier et al., 1995), some fracturing might enhance the lateral distribution of water from the perennial aquifer in Pajarito Canyon. Anisotropy in hydrologic properties could also contribute to lateral flow from the canyons.

These simulations do not include the alluvial layers that blanket the floors of both canyons (Turin, 1995). In our simulations, the high saturation boundary conditions, which represent the canyons, are applied directly to the top of Unit 2a and result in predominantly downward flow. As shown in Figure 5, the high saturation zones below the canyons are fairly localized beneath the canyons. The alluvial aquifer could distribute the water differently resulting in a more lateral infiltration pattern. The low permeability deep basalts might also act as a permeability barrier causing some spreading

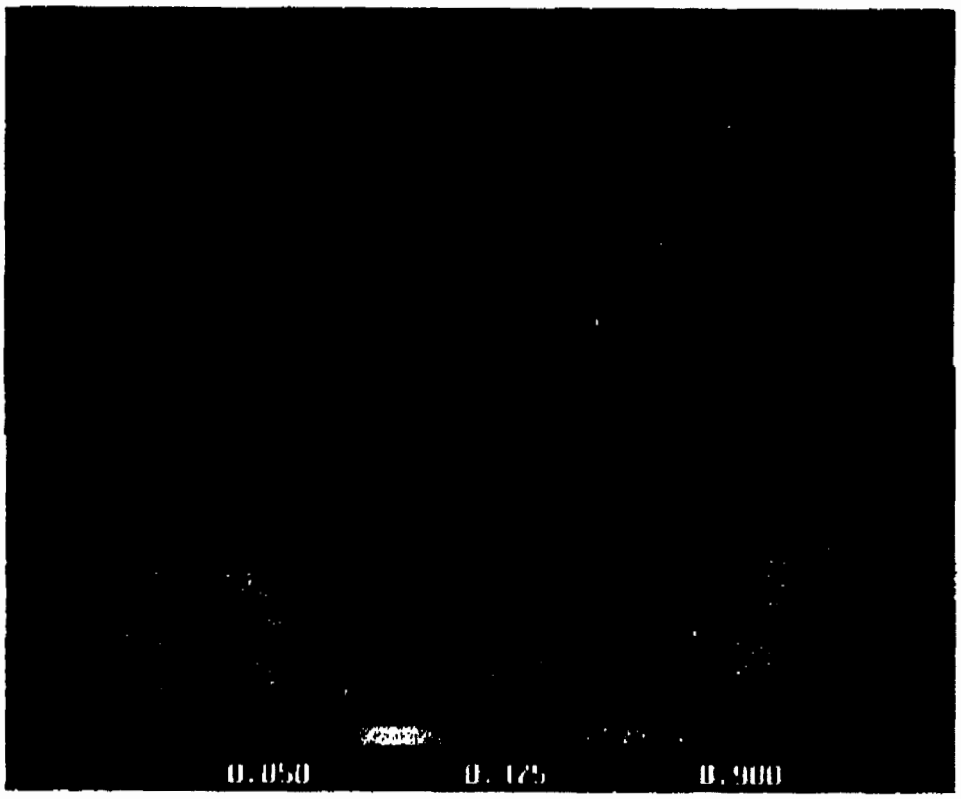

Figure 5. Saturation Profiles for Infiltration at 1 mm/yr with a) No-flow boundaries along canyons, and b) Canyon saturations fixed at 0.9 in Pajarito Canyons and 0.5 in Cañanda del Buey.

of the high saturation plume at the upper interface of this unit. Because of a lack of hydrologic property data for the deeper units, these processes were not investigated. One other detail that is not included in these simulations is that the alluvial aquifer runs normal to the two-dimensional grid. Water in the alluvial aquifer may run down the drainage rather than infiltrating as it is forced to do in this simulation. The question of increased flow rates due to infiltration from the canyons should be revisited in the future when more data concerning the alluvial layers and the hydrologic properties of the deeper units become available.

Response Time to Changes in Surface Infiltration

Infiltration at MDA G is not the steady process shown in the previous calculations. Some sensitivity runs are presented here to determine the system response time to a short-term variation in the steady, infiltration rate. The system is perturbed by varying the steady infiltration rate for a period of 5 years, and monitoring the saturation pulse as it moves through the system. Three variations are examined and in each case the infiltration rate returns to its steady value after the 5-yr deviation: steady infiltration at 0.001 cm/yr with a 5-yr pulse at 1.0 cm/yr, steady infiltration at 0.1 cm/yr with a 5-yr pulse at 1.0 cm/yr, and steady infiltration at 0.1 cm/yr with a 5-yr pulse at 0.001 cm/yr. The steady infiltration results show that the saturation in the deeper units seem to be the result of higher infiltration than in the mesa-top units. These runs are intended to answer the following questions: are the high saturations at depth the results of a previous short-term period of high infiltration, or are the low saturations in the mesa the result of a more recent short-term period of low infiltration? The results of these calculations are fairly inconclusive because the 5-yr duration for the deviation in infiltration rate was not long enough to capture the large discrepancy in the upper and lower saturation profiles. We will, however, discuss the results because they illustrate the extremely slow response time of this system under matrix flow conditions.

The results for the lowest, background infiltration rate (0.001 cm/yr) followed by a 5-yr pulse at 1 cm/yr show that the pulse moves extremely slowly through the upper layer, Unit 2b, taking more than 1500 yrs to move through. Finally after 2000 yrs, a higher saturation is seen in Unit 2a. The background infiltration rate in this case is too slow to force the pulse into the deeper units, rather the pulse is damped out before reaching the units below Unit 2a.

The results for a higher, background infiltration rate (0.1 cm/yr) followed by a 5-yr pulse at 1 cm/yr show that the pulse moves more quickly through Units 2b and 2a. After 500 years, a slight increase in saturation develops in Unit 2a, and at the Unit 1b/1a interface. By 1000 years, the pulse causes a slight increase in saturation in the Otowi Member (0.193 vs. 0.192).

The results for a higher, background infiltration rate (0.1 cm/yr) following by a 5-yr very low infiltration rate (0.001 cm/yr) show a very slight decrease in saturation in Unit 2b for the first 300 years. After 500 years, the saturation profile returns to that for the background infiltration rate.

The results of these three simulations indicate that a short duration deviation in infiltration rate can not explain the apparent discrepancy in saturation between the mesa top units and the sub-mesa units. We think that a previous long-term (maybe 100's to even 1000's of years) high infiltration event followed by a more recent (or current) long-term low infiltration event could better explain the site saturation data. This suggests a climate change scenario that could be further examined through field and modeling studies. The system response is very slow as indicated by these runs and by the very long simulation times (about 50,000 to 500,000 years) required to achieve steady state flow in the base case simulations. We do not believe that the large discrepancy in saturation data between the mesa-top and deeper units can be explained by normal yearly fluctuations in infiltration rate if the system is controlled strictly by flow through the matrix material. Deep infiltration through fractures is considered later in this report.

Sensitivity to Saturated Hydraulic Conductivity

The hydrologic properties used in these simulations assume homogeneous, isotropic properties for each unit. Data from core samples (Krier et al., 1995) show that much variability in hydrologic

properties actually exists. Here we present a brief sensitivity analysis to the property saturated hydraulic conductivity, K_{sat}, in the four upper units (Unit 2b, Unit 2a, Unit 1b, and Unit 1a). This analysis also assumes homogeneous, isotropic properties for each unit, but we vary K_{sat} up and down by an order of magnitude in various combinations to determine the effect that uncertainty in K_{sat} can have on the calculated saturation profiles. Seven different cases were run using a steady infiltration rate of 0.01 cm/yr. This flow rate was seen to match the data in Unit 2b, Unit 1b, and Unit 1a quite well, but gives results that are too wet for the measured saturation in Unit 2a. The resulting saturation profiles for four of the cases along with the base case (0.01 cm/yr infiltration) results are shown in Figure 6.

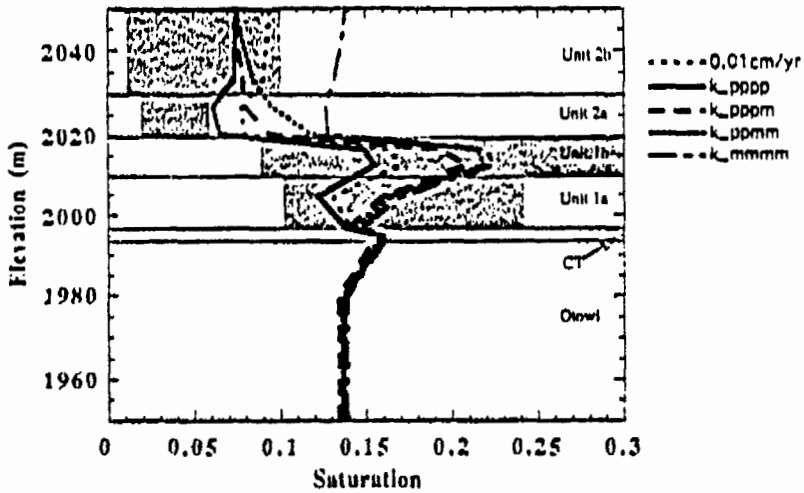

Figure 6. Comparison of site data (gray boxes) to calculated steady-state saturation profiles for several variations in K_{sat}. The infiltration rate is 0.01 cm/yr.

The naming convention for these runs uses a single letter (either p or m) for each unit from Unit 2b down to Unit 1a to signify if the K_{sat} for that unit is either an order of magnitude larger (p) or an order of magnitude smaller (m) than the average for that unit. For example, for Case ppmm, K_{sat} was increased by an order of magnitude for Units 2b and 2a and decreased by an order of magnitude for Units 1b and 1a. The best calculated fit to the average in-situ saturation data at this flow rate occurs for Case pppp where all of the K_{sat} values are increased by an order of magnitude. A higher K_{sat} value allows the steady flow to pass through the system at lower saturations, giving a better overall fit to the data by bringing the calculated saturation closer to the data measured in Unit 2a. A lower K_{sat} in Unit 1a or in both Unit 1a and Unit 1b forces the saturation up in both units for a given steady flow rate, which still matches the data in these two units, but also forces higher saturations in Unit 2a which is undesirable in terms of matching the data. Note that although Case pppp matches the data well through Unit 1a, the profile is much too dry to match saturation data for the Cerro Toledo and Otowi Member (see Figure 3).

This modeling assumes that each unit in homogeneous. The true system is actually quite heterogeneous, and water may flow preferentially through a path with higher K_{sat} resulting in an overall lower saturation. This influence could partially explain the very low saturations in Unit 2a and Unit 2b, but would work against the higher observed saturation values in the deeper units. Here again, we don't believe that the apparent discrepancy in saturation between the mesa-top units and the deeper units can be explained fully by uncertainty in the values for the matrix, saturated-hydraulic conductivity.

PART II - A STUDY OF SPECIFIC FLOW PROCESSES

Fracture Flow

We have performed another study using FEHM to analyze the influence of different characteristics of a fractured system on the movement of fluids in the subsurface. The study focuses on conditions that are relevant to our local system, particularly the influence of fracture coatings and fracture fills on infiltration of water, and on the extent of matrix-fracture communication. This work is described in full by Soll (1995) but the results are summarized here as they pertain to the development of the flow model for MDA G.

In an attempt to isolate behaviors, we have chosen a system that is a single vertical fracture centered in an otherwise uniform block of matrix (Figure 7). There are four parts of the system: the matrix, the fracture, the fracture coating and the fracture fill. The matrix characteristics represent Bandelier Tuff properties from Mesita Del Buey, Unit 2a. The fracture aperture and spacings are average values from local measurements (Krier et al., 1995). In this study the fracture is given the hydrologic properties of a highly porous and highly permeable sand. This assumption allows us to study a fractured system using a porous media simulator, but the results must be interpreted in context with field observations and measurements.

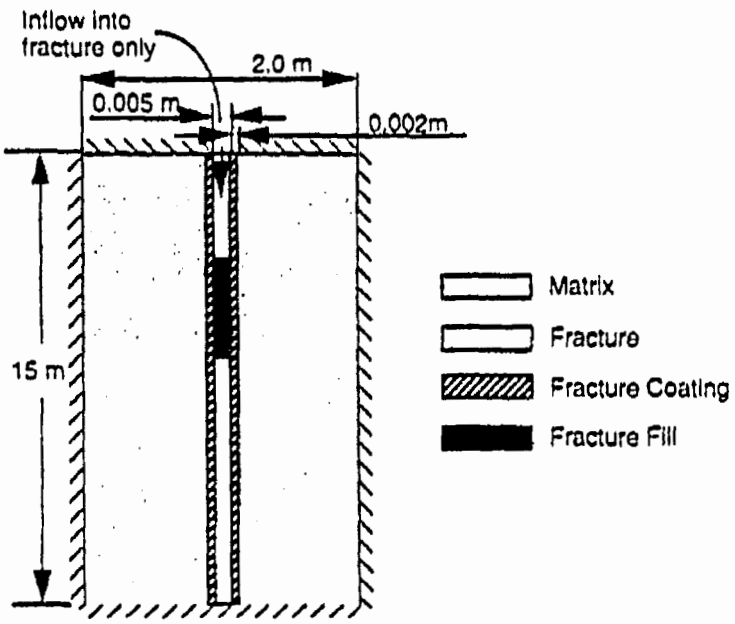

Figure 7. System Configuration for Fracture Flow Study.

The system is discretized such that a thin coating layer can be assigned along the walls of the fracture. For simulations where no coating is present these elements are assigned matrix properties, thus maintaining the 5-mm fracture aperture through all simulations. Fracture fill can be emplaced by replacing the fracture's hydrologic properties with fill properties for some given length of the fracture. When present, fracture coatings and fracture fills are assigned clay parameters. We use clay parameters from the literature because there are no values available for the local clays and caliches.

Two different inflow conditions are used at the top of the fracture. One inflow condition assumes a constant influx, at a rate of 5 cm/day, which we considered to be representative of an extreme event for a single day. However, this inflow rate was applied for the entire time period of the simulations, often up to 100 days. The other inflow condition used was a ponded condition at the top of the fracture applied for 0.5 days, followed by removal of the source. This was effectively an infinite source of water for 0.5 days with infiltration rates controlled by the fracture-matrix system. Both of these inflow conditions result in an amount of water entering the system in a matter of days that far exceeds the amount of precipitation seen at Los Alamos over a period of years. These extreme conditions allow us to focus on absolute worst cases.

The most dominant observation from the simulations is that in all but the most extreme infiltration events, fractures in the Bandelier Tuff of MDA G do not appear to provide a 'fast flow path' for liquids. Even under extremely high infiltration events, fractures with no coatings or fills are not able to carry liquids very far, and the invading saturation front looks very similar to that observed in a non-fractured system with point injection.

We found that the effect of a coating along the walls of the fracture is dependent on the relative conductivities of the coating and the matrix. A coating with only 2 orders of magnitude less conductivity than that of the matrix does virtually nothing to prevent liquid in the fracture from being imbibed by the matrix. When there is a larger (4 orders of magnitude) reduction in conductivity at the fracture-matrix interface, water is strongly channeled in the fracture. Any conductivity reduction acts to spread the infiltrating front further down the matrix, allowing water to penetrate deeper during an infiltration event. However, a discontinuity in the low conductivity coating interrupts the fast flow down the fracture. This suggests that the high capillarity of the Bandelier tuff will rapidly draw water into the matrix near any break in a fracture coating. The simulations also show that fracture flow driven by the ponded boundary condition ceases once the source is removed.

When we consider the role of fills in affecting water infiltration, we find that fractures that are filled at the exposed surface of the fracture are effective barriers to inflow into the fracture. These observations are in agreement with Rosenberg et al. (1993). Fills below the surface are effective barriers to continuous flow down the fracture. With no coating or only minimal conductivity reduction above the fill, water entering the fracture is simply imbibed into the matrix and proceeds down as matrix flow. When a continuous, low conductivity coating is present, the water does not pass beyond the fill, and simply ponds at the surface. A fracture that ends within a unit, or at the interface between two units will behave like a fracture that is filled at that level. The path for the water in the fracture is eliminated, and the water must find an alternate route through the subsurface.

We have also run a simulation where a 1 meter "cap" of matrix material is placed across the entire fracture-matrix system. This condition represents the current surface cap at MDA G and the conditions at the floor of the waste disposal pits. The matrix cap was then held at saturations ranging from 50% to 90%. In none of the simulations did water break into the fracture, although it moved as a steady front through the remaining matrix material. These results are consistent with results obtained by Rosenberg et al. (1993) using a different numerical model.

Although most of these results indicate that fractures do not play a significant role in moving water from the surface to the water table, there are reasonable, possible local conditions that may be sufficient to produce significant flow. There are high influx conditions such as snow melt or large runoff events that could cause water to move a significant distance in a fractured system. There is some evidence for such flow at other LANL locations (Turin, 1995). It must also be kept in mind that there is wide variation between the different fractures, and that it is possible for one or two fractures to be carrying water while most others do not.

We do not expect fractures to be a fast path for contaminants out of the bottom of the pits because these fractures are covered with crushed tuff. However, if water is able to pond within the pit it may be possible for that water to exit the pit through fractures on the face of the pit, which are not filled or covered. Fractures that are not directly beneath the pits may play an indirect role in the movement of water and contaminants from the pits. Increases in matrix saturation as a result of water moving in the fractures are a potential source of water beneath the pits. As observed in the simulations, water that enters the matrix rapidly redistributes throughout the matrix block toward a uniform saturation. This can act to increase saturation beneath the pit, thus raising the hydraulic conductivity and allowing more rapid movement through the matrix.

Evaporation from Mesa Sides, Fractures, and Surge Beds

Very low net infiltration rates are required to match the field observed saturation in the two mesa-top units, Units 2b and 2a. Evaporation from the top and sides of the mesa and possibly from fractures is a likely player in keeping the mesa dry. Some data (Rogers et al., 1995) suggest that groundwater flow may be upward toward the volcanic surge beds located at the base of Unit 2b. This flow could be driven by evaporation occurring in the surge beds. Some simple simulations are used to study these effects.

First we consider evaporation from the mesa sides and from vertical fractures with both 10-m and 5-m fracture spacing. A two-dimensional rectangular grid (25 m wide, 5 m tall) composed of a homogeneous material, either Unit 2b or Unit 2a, is used. Figure 8 shows the problem set up. Uniform infiltration of 0.1 cm/yr occurs along the upper boundary. This infiltration rate accounts for evaporation from the mesa top, but is higher than the flow rates found previously to best match the in-situ saturations of Units 2b and 2a (0 to 0.001 cm/yr). We compare the resulting vertical saturation profiles for the following cases: infiltration only, infiltration with evaporation occurring along the right boundary (mesa edge), and infiltration with evaporation along the right boundary and from fractures of either 10-m or 5-m spacing. For the infiltration only case, the right boundary is impermeable. The evaporative boundary is modeled by fixing the saturation at that boundary to a low saturation corresponding to 50% relative humidity. For the fracture runs, the fractures are also held at a low saturation corresponding to 50% relative humidity. The corresponding saturation values are 0.032 for Unit 2b and 0.00892 for Unit 2a.

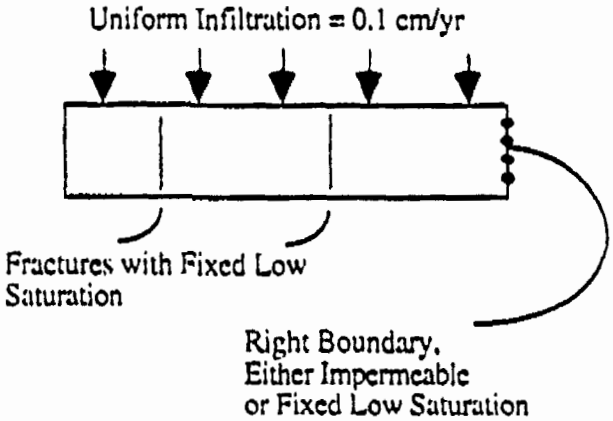

Figure 8. Problem set-up for study of evaporative effects from mesa sides and from fractures.

Figures 9 and 10 show the simulated saturation profiles for a horizontal slice through the center of the grid for Units 2b and 2a respectively. For both units, it appears that evaporation affects the saturation profile to a distance of about 7 m from the mesa edge; not much for a mesa that is over 300 m wide. However, assuming that fractures with 5-m spacing act as conduits for air flow, evaporative effects may decrease saturations throughout both units in the mesa top. With fractures spaced 5 m apart, average saturation decreases by ~0.05. From Figure 3 we see that this order decrease in saturation corresponds to approximately an order of magnitude decrease in the net steady infiltration rate. Actual fracture spacing in these units is 1.0 to 1.3 m, but only a fraction of these may be flowing. Some low air flow is required to remove water vapor from tuff, as the relative humidity of the air in a non-flowing fracture would equilibrate with that of the surrounding matrix. It is quite possible that fluctuations in the barometric pressure (Nilson et al., 1991), thermal gradients, and topographic effects (Weeks, 1987) could drive such air flow in a fractured system located on a mesa top.

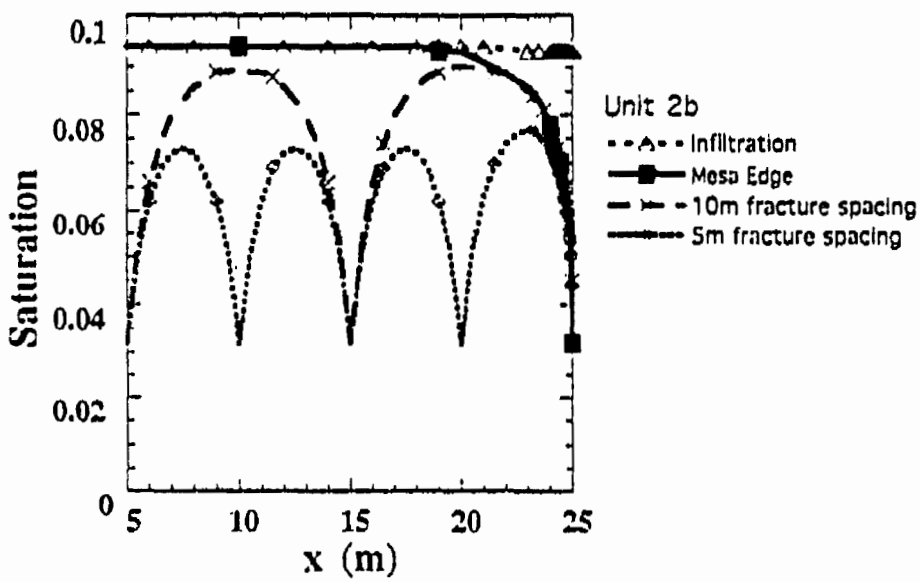

Figure 9. Resulting Saturation Profiles for Evaporation along a Mesa Edge (right side) and from fractures with 5-m and 10-m spacing, Unit 2b.

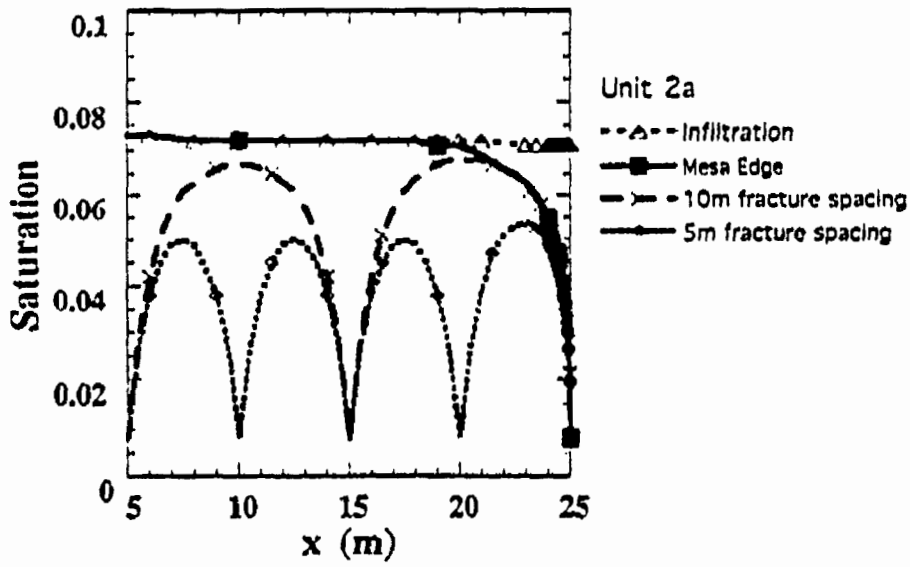

Figure 10. Resulting Saturation Profiles for Evaporation along a Mesa Edge (right side) and from fractures with 5-m and 10-m spacing, Unit 2a.

We note here that evaporation in these simulations and the one that follows is modeled as an isothermal process with saturations fixed at low values corresponding to a relative humidity of 50%. These results are nearly identical to simulated results, also calculated with FEHM, under non-isothermal conditions which account for vapor pressure lowering and binary diffusion of air and water vapor. For these examples, evaporation results in a simple capillary pressure driven wicking toward the drier, atmospheric boundary. Water vapor contributes less than 1% of the mass in the system for these particular examples which were held at or very close to 20°C, even for the non-isothermal simulations. However, the more complex processes may have a larger effect under more realistic non-isothermal conditions (e.g., geothermal gradients or solar heating of the mesa sides).

The next example examines the hypothesis that air flow through the surge beds located at the base of Unit 2b can cause upward moisture flux from Unit 2a. Two layers, Units 2b and 2a, are modeled with their appropriate hydrologic properties and thicknesses. Uniform infiltration at a rate of 0.1 cm/yr is applied along the upper boundary. Again we compare the results with infiltration alone to results which include evaporation along the "surge bed". The surge bed is modeled simply as a set of low saturation nodes, corresponding again to a relative humidity of 50%, along the interface of the two layers. Figure 11 and 12 show the steady-state saturation and capillary pressure profiles for this case. Saturation values throughout both units are significantly lowered by the fixed low saturation at the interface. In Figure 12, the calculated values are compared to suction data reported by Rogers et al. (1995) for Borehole G-5, which is located at MDA G. The data are translated spatially to force the surge bed to align with that from the simulation. We see that the calculated capillary pressure lies between the two data sets reported by Rogers.

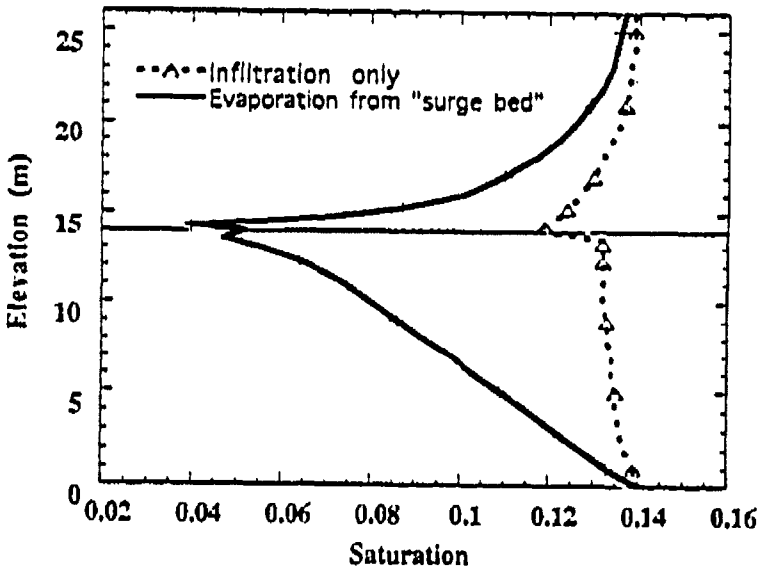

Figure 11. Resulting saturation profile for evaporation along the "surge beds" at the Unit 2b/2a interface compared to that for infiltration alone.

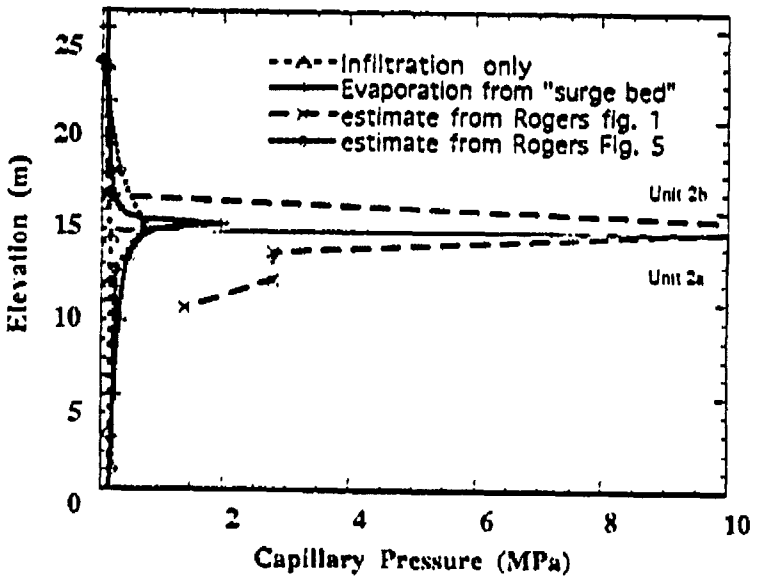

Figure 12. Resulting capillary pressure profile for evaporation along the "surge beds" at the Unit 2b/2a interface compared infiltration alone and to data from Rogers et al. (1995) for Borehole G-5.

These simulations show that evaporation along fractures and surge beds can contribute to significant drying of the mesa top units, possibly causing the very low saturations seen in these units. We feel that the mesa may act as a "natural dry barrier" which contributes near zero net infiltration to the units below the mesa during the "normal drying state" described in the conceptual model. This theory needs to be substantiated with more data and modeling studies.

PART III - POST-DISPOSAL FLOW MODEL

Summary of Findings From Part I and Part II

Simulations assuming low, steady infiltration ($\lesssim$ 1 mm/yr) into the mesa yield saturations that are consistent with those measured at TA-54. However, no single infiltration rate produces a saturation profile that matches the measured saturation data as a function of depth. There is an apparent discrepancy in saturation between the two units that make up the mesa top (Units 2b and 2a) and those below. The limited number of calculations presented here do not indicate that the discrepancy is due either to unsteady matrix flow conditions or to variations in K_{sat} values. The mesa top units are so dry that their saturations seem to be controlled by evaporative effects. We feel that saturations in the sub-mesa units result from additional sources of water to these deeper units - possibly periodic infiltration from a few flowing fractures, infiltration of run-off in the flatter areas that make up the canyons (not considered as part of this study), infiltration from the alluvial aquifers in the canyons or some other unidentified source such as an upgradient recharge area.

Effect of Disposal Pits

The site flow model requires some modification to account for the disposal pits which alter both the subsurface hydrology and the upper boundary condition. The disposal pits are dug from the surface into Unit 2b and some extend into Unit 2a. They are backfilled with crushed Bandelier Tuff. Pit emplacement destroys any fractures within the pits themselves and disturbs the site's natural fracture network.

Here we speculate regarding the effects that the emplacement of these pits has on the subsurface hydrology of the site. Several hydrologic effects may change due to the disruption of the fracture network. First, less evaporation (than background) will take place in the pits themselves because they are now unfractured. Less evaporation may also occur in the intact tuff that immediately surrounds the pits because some fracture connections are broken. Pit emplacement also disrupts the natural vegetation, which curbs transpiration from the site. Over time, these factors could result in higher net infiltration rates, which would yield higher saturation values in the mesa top units than those currently observed.

Next, since fractures don't run through the pits themselves, instances of episodic fracture flow that may have occurred at these locations will be disrupted. The addition of crushed tuff to the upper and lower surfaces of the pits should also help curb any fracture flow into or out of the pits. These factors could however cause more uniform infiltration into the subsurface. Fractures adjacent to the pits could still potentially transport water, but it is unlikely that they would pick up waste from the pits, which the modeling results show moves predominantly downward.

The pits extend to the bottom of Unit 2b, and in some cases into Unit 2a. Transport of waste from the pits should be dominated by the flow field in the crushed tuff rather than that in the intact Unit 2b tuff. Deep percolation estimates for the pits performed by Springer (1995) result in a average rate of 3.8 mm/yr. This estimate is for a base case calculation using estimates for precipitation, surface run-off, interflow, and evapotranspiration and contains much uncertainty (Springer, 1995).

Resulting Flow Model

The resulting flow model is based on the two-dimensional steady simulations presented in Part I of this paper. The cross section is modified as shown in Figure 13 to include five disposal pits, Pits 32, 35, 36, 37, and 38. These pits are approximately located within the cross section that is modeled, and are taken to be representative of a typical disposal area. Because the disposal pits are backfilled with crushed Bandelier Tuff, the computational nodes associated with the pits are assigned hydrologic properties for crushed tuff. These values are (Springer, 1995): $K_{sat} = 2.89 \times 10^{-4}$ cm/s, porosity = 0.3308, $\theta_r = 0.01$, $\alpha = 0.1433$ cm^{-1}, and n = 1.506.

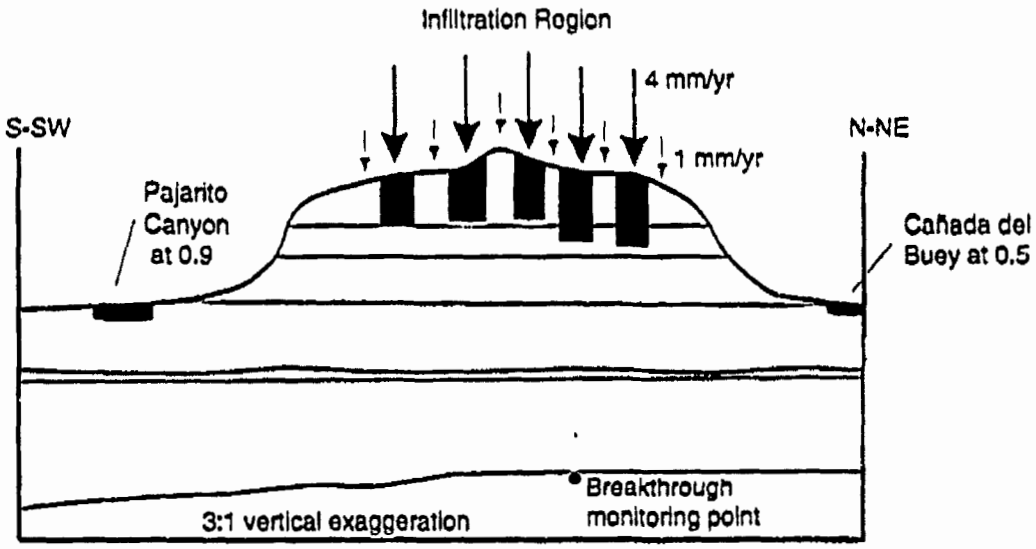

Figure 13. Two-dimensional cross section used for numerical simulations, modified to indicate five waste disposal pits.

We assume a steady infiltration rate of 1 mm/yr over undisturbed portions of the mesa top and include increased saturations along the canyon floors. Infiltration into the pits is assumed to be 4 mm/yr, based on Springer's (1995) estimate. We feel that the 1 mm/yr flow rate yields a good match to saturation data in the sub-mesa units. This flow rate is much higher than that required to match saturation data in the mesa-top units, but transport in these units is likely to be dominated by the 4 mm/yr infiltration rate assumed for the disposal pits. Increased saturations are included along the canyon floors in the event that some nuclides diffuse laterally and are affected by the faster flow field beneath the wetter canyons. The calculation is run to steady state using the boundary conditions described above. The resulting two-dimensional saturation field is shown in Figure 14. This can be compared to the saturation field for the "background" canyon simulation (Figure 5b), and the increased saturation associated with the pits is easily identified. We must point out that our modeling takes no account for flow and transport times through the lower three units (Guaje Pumice, Cerros del Rio Basalts, and Puye Formation) because so little data exist for these units. These three units account for approximately 70% of the unsaturated zone as shown in Figure 1.

To summarize, the difference between this flow model and the background flow model is that the infiltration rate into the five pits is increased (4 mm/yr vs. 1 mm/yr), the pits are given crushed tuff hydrologic properties, and increased saturations are included along the canyon floors. The resulting steady flow field forms the basis for vadose-zone transport calculations that are presented in the remainder of this report. We were concerned that since the 4 mm/yr pit infiltration rate represents a "new" boundary condition for the system, the transport simulations might be sensitive to the propogation of this boundary condition through the system. Results for transport simulations using both the steady flow field just described and a transient flow field (where the 4 mm/yr flow rate is applied to the previous steady, flow field using the 1 mm/yr boundary condition along the upper surface) showed that the transport results are not sensitive to the propogation of this wetting front. From this, we concluded that little error is induced by assuming that the pit infiltration rate of 4 mm/yr is in equilibrium with the background flow field rather than being a "new" transient boundary condition.

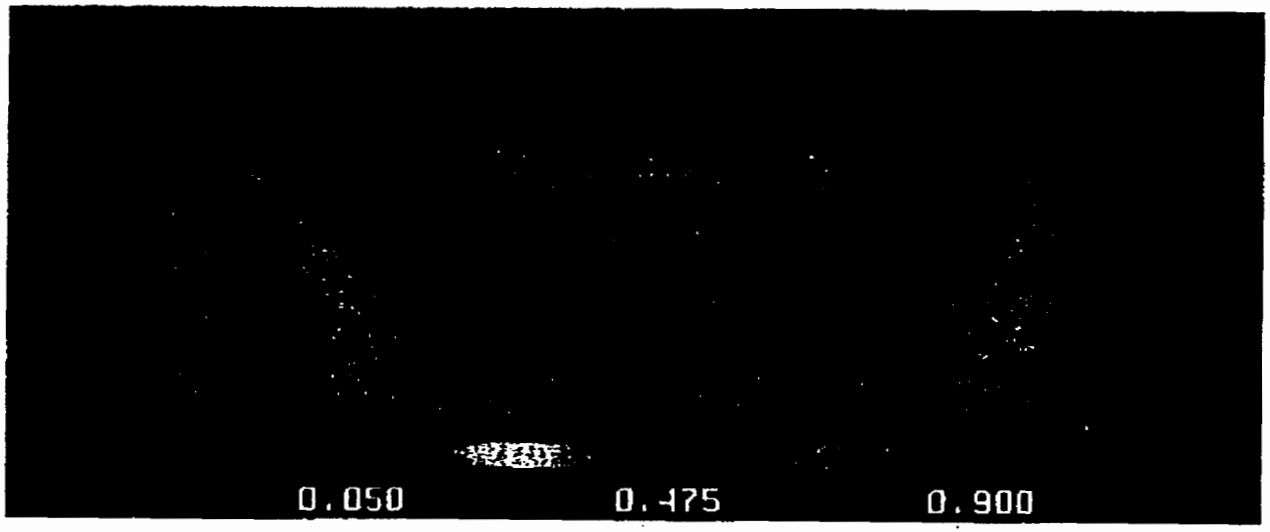

Figure 14. Saturation Profile for the Steady-state, Post-Disposal Flow Model of MDA G.

PART IV - TRANSPORT MODELING

Modeling Approach

The post-disposal, steady flow model developed in the last section forms the basis for the transport model. A concentration breakthrough curve is developed for each parent nuclide and its daughter products. This breakthrough is monitored at a point located at the top the Cerros del Rio Basalt formation as shown in Figure 13. This point was found to receive both the earliest breakthrough and the highest concentrations because of its location beneath the two deeper pits and beneath a cluster of closely-spaced pits. We ignore transport through the basalt unit and the Puye Formation because of the uncertainty associated with calculating flow through these units.

Time dependent source terms, provided by Vold (1995), are used to simulate the total release of the various radionuclides that make up the historic inventory, which is defined as waste buried between September, 1988 and December, 1994. Future calculations will also consider the legacy waste disposed of at MDA G between 1957 and 1988 (Hollis et al., 1995). Each source term is represented in tabular form as a flux term (i.e., moles/yr). The source is divided uniformly, based on pit volume, between the five pits in the modeled cross section. The historic source term is defined for each parent nuclide at the same 45 time values through 50,000 years. For simulations which run longer than 50,000 years, the source term drops to zero after 50,000 years (except in the cases of Hf-182 and Th-232 which are discussed later). Linear interpolation of the source term table is used between table entries. Time stepping within FEHM is controlled so that the source term is sampled several times within each set of adjacent table entries. This insures that the correct inventory is input to the simulations.

Transport properties for both the porous media and the radioactive species are required. These properties include effective diffusion coefficients, dispersivity values, sorption coefficients, and radioactive half-lives. The diffusion coefficient is a function of both the radionuclide and the porous media. The radionuclide has its own diffusion coefficient in water. However, within a porous medium, the diffusion coefficient decreases substantially because its path becomes quite tortuous. A single diffusion coefficient of 10^{-10} m^2/s was used for all of the nuclides, which assumes a molecular diffusion coefficient of 10^{-9} m^2/s and a tortuosity of 0.1. A dispersivity value of 1.0 m was also used. The sorption coefficient, Kd, reported for each nuclide on tuff (Krier et al., 1995) was used in the pits and the rock layers from Unit 2b down through the Otowi Member. A Kd value of zero was assigned to the basalt unit because we are taking no credit for retardation in the basalt. This means that the liquid concentration reported at the top of the basalt represents the full dose reaching that point. The appropriate half-lives for each species (Vold, 1995) are also used.

Generic Source Term

A generic source term was used in order to perform scoping transport calculations. This source was used to study the effect of the sorption coefficient (Kd) on transport times for a non-decaying species to the top of the basalts. These results are useful for confirming that subsequent, more complicated results for decaying species are calculated correctly, and also for narrowing the list of nuclides that require full transport calculations. Figure 15 shows the time-dependent, generic source term, as well as a plot of concentration vs. time for 5 different Kd values: 0.0, 0.3, 1.0, 2.0, and 10.0. We examine two characteristics for each of these curves: 1) arrival time for the peak concentration, and 2) first arrival time, which we define to be the arrival time for a concentration that is 1% of the peak value. Table 2 gives results for time to peak concentration and first arrival vs. Kd for these 5 Kd values.

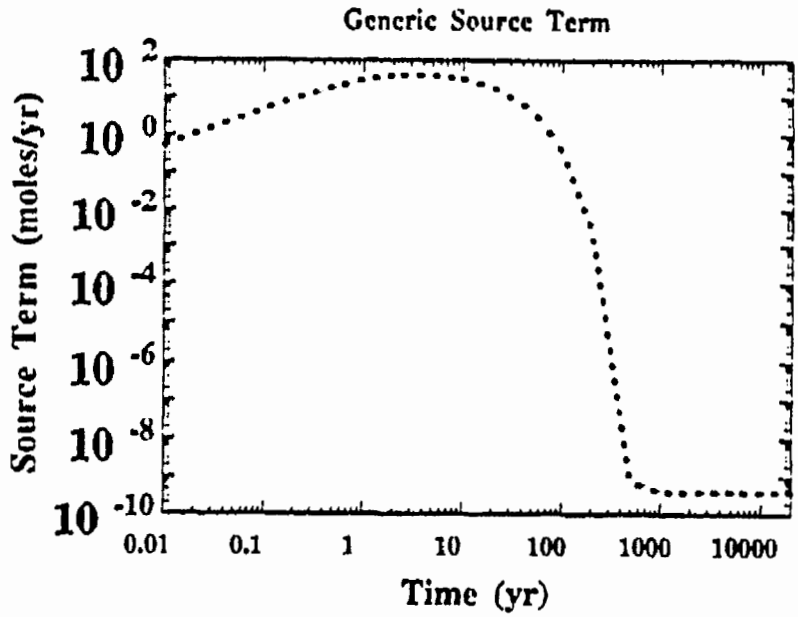

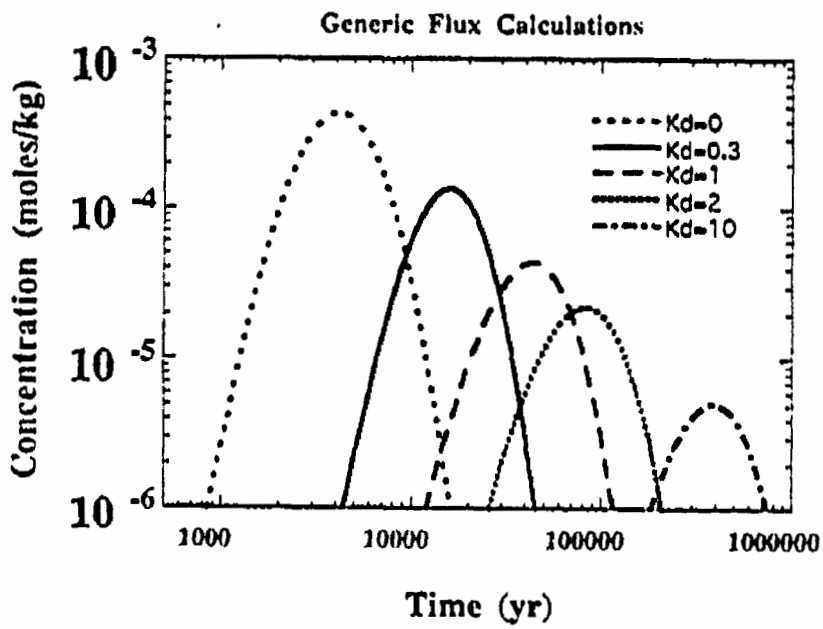

Figure 15. (a) Time dependent, generic source term and (b) Concentration breakthrough curve for generic source term assuming different Kd values.

Table 2. Times to peak concentration and first arrival as a function of Kd for the generic source term.		
Kd	Time (yr) for Peak Concentration	Time (yr) of First Arrival
0	4,200	1,100
0.3	16,000	4,600
1.0	44,000	10,000
2.0	79,500	21,000
10.0	395,000	99,000

Peak arrival time can be estimated for larger Kd values by multiplying the retardation factor, R, by the time to peak concentration for a non-sorbing species.

$$R = 1.0 + Kd(\rho_b/\theta)$$

Here ρ_b is the bulk density and is approximately 1.2 g/cm^3 for the tuffs at the site. θ is the moisture content. A value of 0.13 for θ is close to site data and produces results that are consistent with those presented in Table 2. For large Kd, we can estimate R = 9.2 x Kd, and the arrival of the peak as R x 4200 years. This same concept also works well for estimating the time of first arrival (e.g. 1% of peak concentration) as R x 1100 years. Table 3 gives estimates for the arrival time of the peak and first arrival for Kd values ranging from 20 to 200. We see that large sorption coefficients (e.g., Kd = 40 and above) result in transport times to the top of the basalt in excess of a million years.

Table 3. Estimated times to peak concentration and first arrival as a function of Kd for the generic source term.		
Kd	Estimated Time (yr) for Peak Concentration	Estimated Time (yr) of First Arrival
20	770,000	210,000
50	1.9×10^6	520,000
100	3.8×10^6	1.0×10^6
150	5.8×10^6	1.5×10^6
200	7.7×10^6	2.0×10^6

HISTORIC INVENTORY

A total of 30 parent nuclides were expected to require full transport calculations based on their inventories. Using the results from the generic source runs, the number of nuclides requiring full simulations was decreased to 17. Results for each of the 30 nuclides are given in the following section. These results include the justification for eliminating 13 of the nuclides based on a

screening technique, and the results for the 17 parent nuclides and their daughter products that required full transport calculations.

Screening

The 30 nuclides were screened by comparing their half-lives to their transport times. Of these, 13 nuclides were eliminated based on this screening technique: Ag-108m, Ba-133, Cd-113m, Co-60, Cs-137, Eu-152, Eu-154, Gd-148, H-3, Nb-94, Ra-226, Sm-151, and Sr-90. The screening process compares the half-life to the transport time for first arrival, which is a function of Kd. If twenty times the half-life is less than the transport time for first arrival, the nuclide should have no release to the deep aquifer, because the source concentration has decayed to 1×10^{-6} times its original concentration. If this is the case, the nuclide is eliminated and requires no further calculation unless it is the parent to other long-lived species. Twelve nuclides that were eliminated have no daughters. For the one that has a daughter products, Ra-226, both the parent and daughter have short half-lives in comparison to their transport times. Table 4 gives justification for the screening of these nuclides . The table shows that for every nuclide, the time of first arrival is many times greater than twenty times the half-life.

Table 4. Screening Criteria for Radionuclides.

Radionuclide	Half-life (yr)	20 x Half-life (yr)	Kd	Time (yr) of First Arrival based on Kd
Ag-108m	127	2,540	90	900,000
Ba-133	10.5	210	946	9,000,000
Cd-113m	13.6	272	80	800,000
Co-60	5.26	105	0.45	4,500
Cs-137	30	600	428	4,000,000
Eu-152	12.7	254	50	500,000
Eu-154	16	320	50	500,000
Gd-148	84	1680	50	500,000
H-3	12.3	246	0	1,100
Nb-94	20,000	400,000	100	1,000,000
Ra-226	1600	32,000	200	2,000,000
Pb-210	20.4	408	25	250,000
Sm-151	87	174	50	500,000
Sr-90	27.7	554	116	1,000,000

This estimate for tritium (H-3) transport considers only liquid-phase movement of the species. Tritium can also move in the gas phase as HTO vapor, H_2 gas, or CH_4 gas. Vapor-phase transport of tritium to the surface is considered as part of the Performance Assessment (Vold, 1995). However, vapor-phase transport of tritium to the water table is neglected at this point.

Results of Transport Calculations

Simulation results for the remaining 17 parent nuclides and their daughter products are presented in the following sections. These nuclides are Am-241, C-14, Hf-182, Mo-93, Np-237, Pu-238, Pu-239, Pu-240, Pu-241, Pu-242, Tc-99, Th-232, U-233, U-234, U-235, U-236, and U-238. For all the nuclides except Mo-93, we show the time dependent source and the resulting concentration breakthrough curve. We also present a technique that was used to help verify that each simulation produced results that are correct. Table 5 gives the half-lives (Vold, 1995) and sorption coefficients (Krier et al, 1995) used for the remaining simulations for the historic inventory.

Table 5. Half-lives and Sorption Coefficients required for Transport Calculations

Radionuclide	Half-life (yr)	Kd
Ac-227	21.6	130
Am-241	432	130
C-14	5,730	0
Hf-182	9.00×10^6	500
Mo-93	3,500	4
Nb-93m	13.6	100
Np-237	2.14×10^6	0.007
Pa-231	3.25×10^{10}	50
Pb-210	20.4	25
Pu-238	87.8	110
Pu-239	2.41×10^4	110
Pu-240	6,570	110
Pu-241	14.4	110
Pu-242	3.76×10^5	110
Ra-226	1,600	200
Ra-228	5.75	200
Tc-99	2.13×10^5	0.3
Th-229	7,340	500
Th-230	7.70×10^4	500
Th-232	1.40×10^{10}	500
U-233	1.62×10^5	1.8
U-234	2.47×10^5	1.8
U-235	7.04×10^8	1.8
U-236	2.34×10^7	1.8
U-238	4.47×10^9	1.8

A transport calculation for Mo-93 showed no release to the top of the basalt. Based on its Kd of 4, we expect it to first arrive after about 40,000 years and to peak at about 150,000 years. Twenty times its half-life is 70,000 years, so this nuclide was not eliminated based on the screening

criteria. However, its concentration decays to about 1×10^{-4} its initial value by its expected first arrival and to about 1×10^{-13} its initial value by its expected peak time. Based on this analysis, it is not surprising that we see no release of this species. Its daughter product Nb-93m has a short half-life, 272 years, and also shows no breakthrough.

Am-241

The two figures below show the time-dependent source term and the concentration breakthrough curve for the Am-241 decay chain. Am-241 forms the chain: Am-241 -> Np-237 -> U-233 -> Th-229. The sorption coefficients on tuff and half-lives are given in Table 5. Using the screening technique described above, we expect the Am-241 peak to occur after about 5 x 10^6 years. This time is much longer than its half-life of 432 years, and no release of Am-241 is measured at the monitoring point. We expect to see the Np-237 peak after about 4,500 years with a slight lag of the order of 400 years (about the half-life of Am-241) to allow some ingrowth of this species. The peak occurs at 5,068 years indicating that this result is correct. The U-233 and Th-229 peaks occur shortly after the Np-237 peak. Their concentrations are much lower (4 and 6 orders of magnitude) because of the long half-life of Np-237, 2.14 x 10^6 years. This slow ingrowth of U-233 and Th-229 produces a relatively constant source term for these species which yields breakthrough curves that are relatively flat at long times.

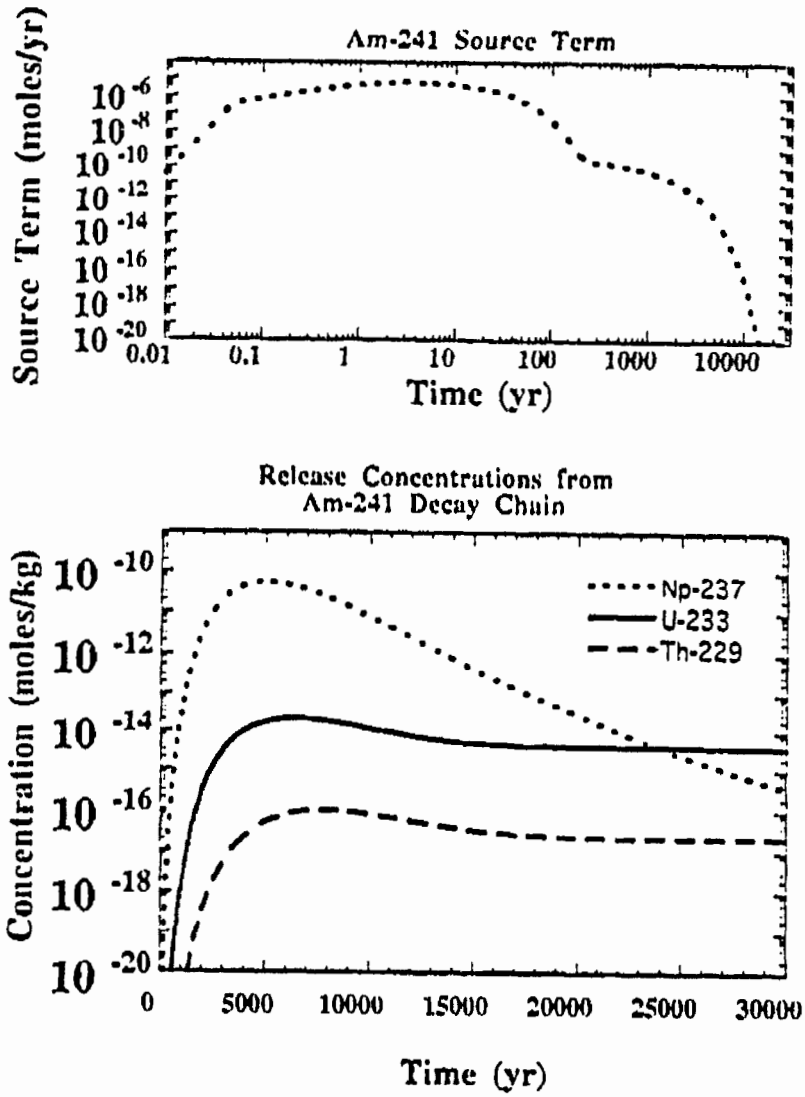

Figure 16. (a) Source term and (b) Concentration breakthrough curve for Am-241.

C-14

The figures below show the time-dependent source term and the concentration breakthrough curve for C-14. C-14 has no daughter products. Here we are treating the C-14 as a water-phase contaminant. Based on its Kd of zero, we expect to see its peak at about 4,200 years. The peak occurs at 3,890 years, which is close to the predicted value. The difference is probably because the C-14 has had some time to decay based on its 5,730 year half-life. We note that C-14 can also migrate as the gases CH_4 and CO_2. Gas-phase transport of C-14 to the surface is included as part of the Performance Assessment (Vold, 1995). We do not include gas-phase transport of C-14 toward the water table.

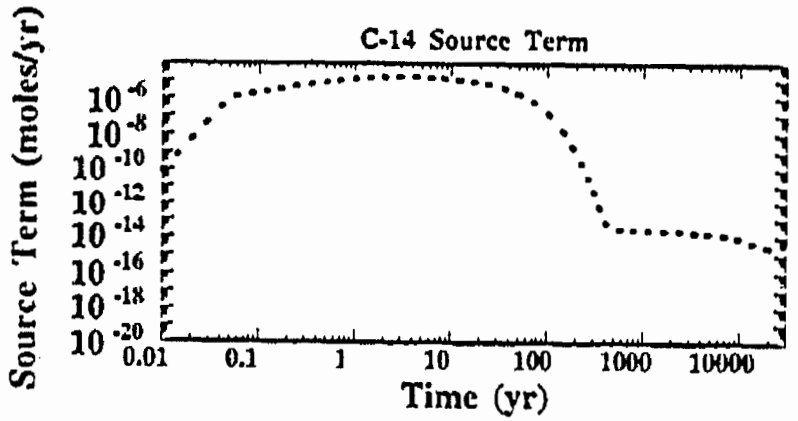

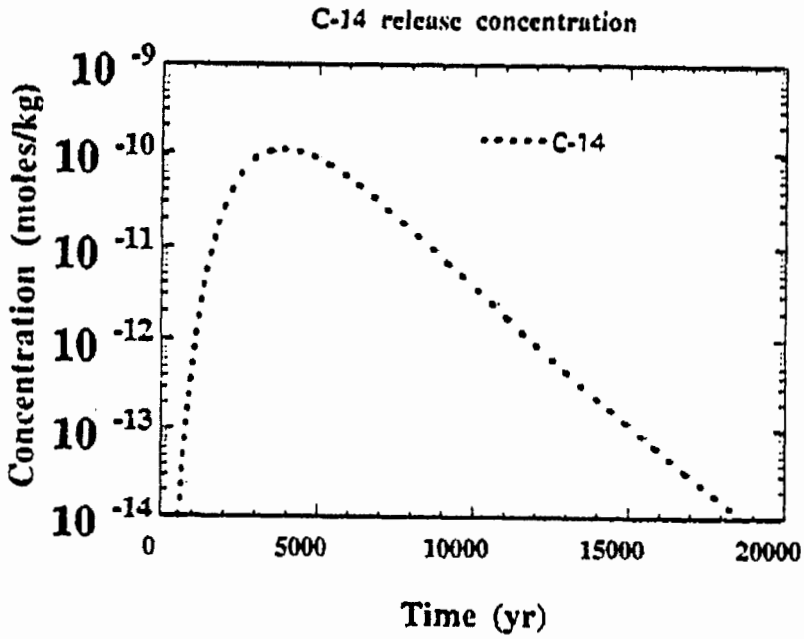

Figure 17. (a) Source term and (b) Concentration breakthrough curve for C-14.

Hf-182

The figures below show the time-dependent source term and the concentration breakthrough curve for Hf-182. Hf-182 forms no daughter products. Its release is solubility limited which leads to a source term that is constant for 1.6 billion years. This constant source produces a flat breakthrough curve rather than a peaked curve as seen for most of the other parent species.

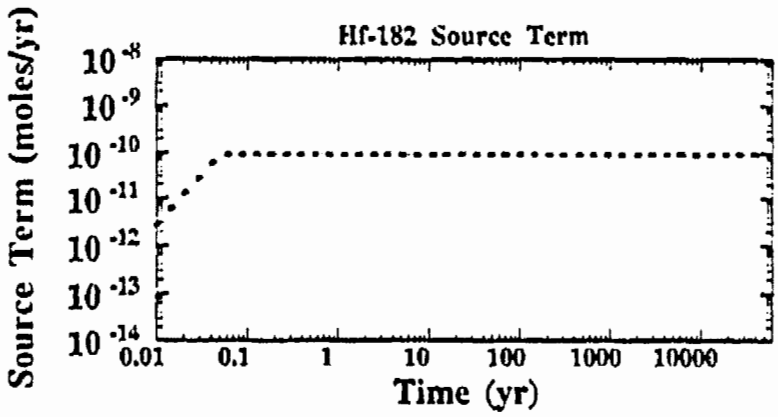

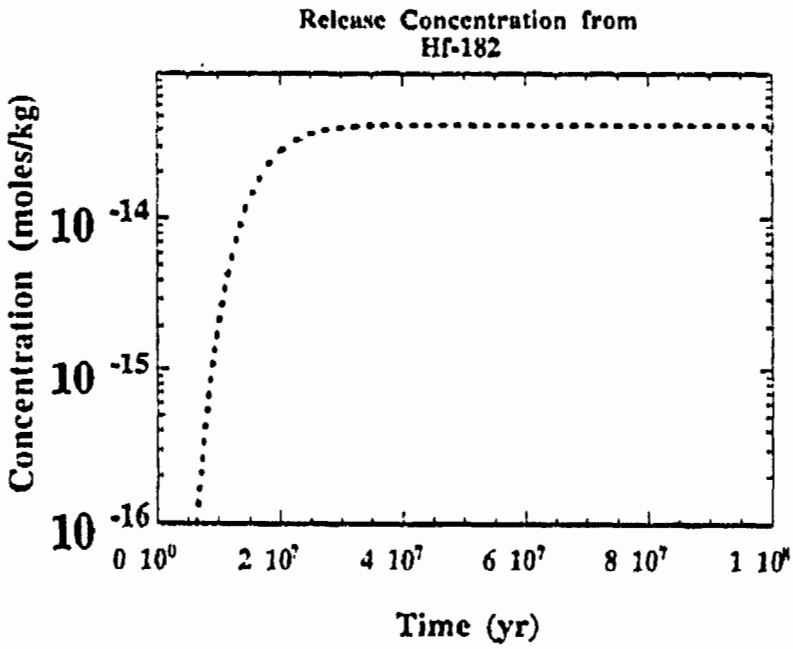

Figure 18. (a) Source term and (b) Concentration breakthrough curve for Hf-182.

Np-237

The two figures below show the time-dependent source term and the concentration breakthrough curves for the Np-237 decay chain. Np-237 forms the decay chain: Np-237 -> U-233 -> Th-229. Based on its sorption coefficient, we expect the Np-237 peak to occur after about 4,500 years, which agrees exactly with the calculated results. Similar to the results for the Am-241 decay chain, the U-233 and Th-229 peaks occur shortly after the Np-237 peak with much lower concentrations and flat tails because of the long half-life of Np-237.

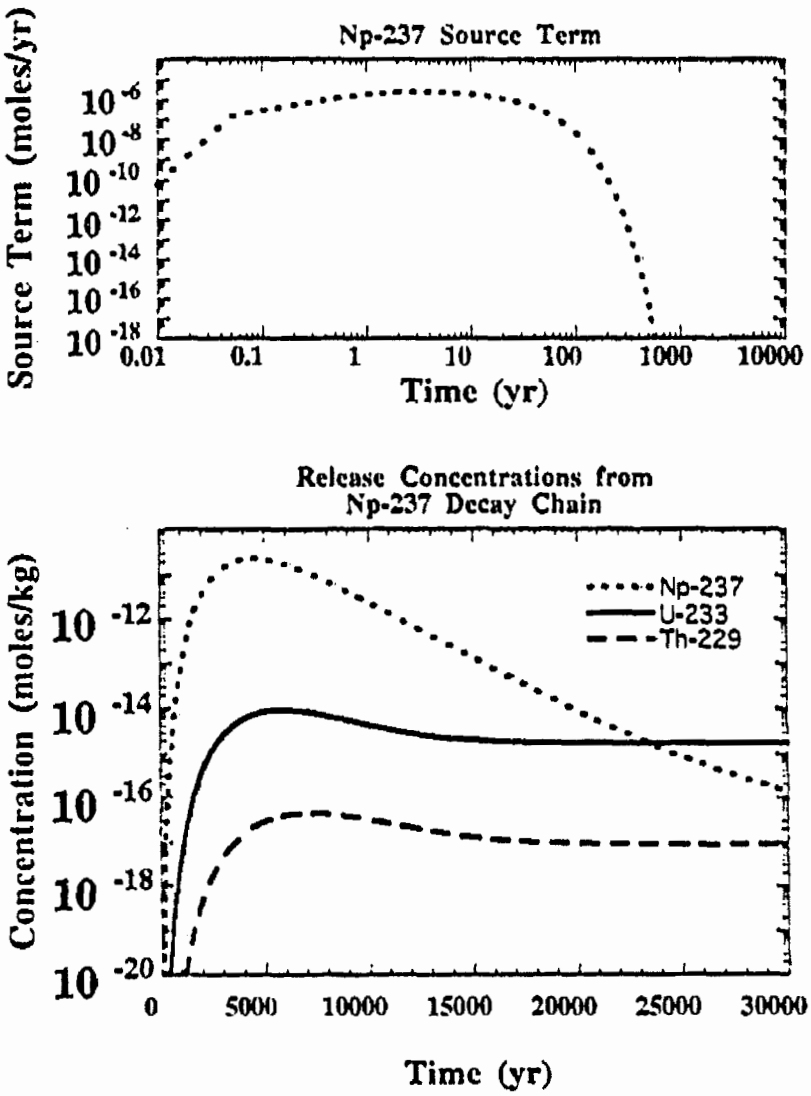

Figure 19. (a) Source term and (b) Concentration breakthrough curve for Np-237.

Pu-238

The time-dependent source term and concentration breakthrough curve for the Pu-238 decay chain are shown below. Pu-238 forms a decay chain: Pu-238 -> U-234 -> Th-230 -> Ra-226 -> Pb-210. Because of the short half-life of Pu-238 (87.8 years), the parent does not break through to the basalts. We expect to see the U-234 peak after about 70,000 years with almost no lag time to allow for ingrowth of this species. The peak occurs at 70,950 years indicating that this result is correct. The Th-230, Ra-226, and Pb-210 peaks occur shortly after this. The tails on the breakthrough curves for these last three daughter products decrease because their half-lives are short in comparison to the simulations time of 300,000 years.

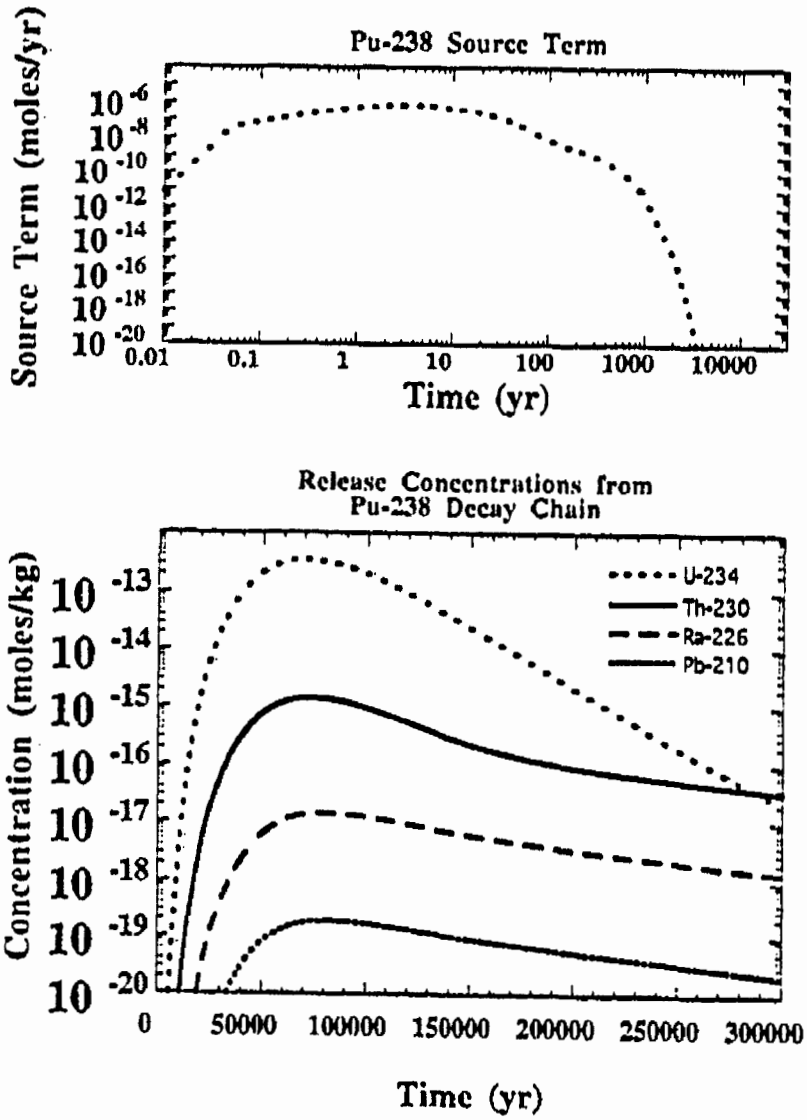

Figure 20. (a) Source term and (b) Concentration breakthrough curve for Pu-238.

Pu-239

The two figures below represent the source term and concentration breakthrough curves for the Pu-239 decay chain. This nuclide forms the decay chain: Pu-239 -> U-235 -> Pa-231 -> Ac-227. Based on its Kd of 110, we don't expect the Pu-239 peak for over 4 million years, at which time it has decayed away, and no release occurs for the parent of this chain. The U-235 peak should occur 70,000 years after a lag time of about 24,000 years (approximate half-life of Pu-239) to allow for ingrowth. The calculated peak occurs at 97,950 years indicating that the simulated results are correct.

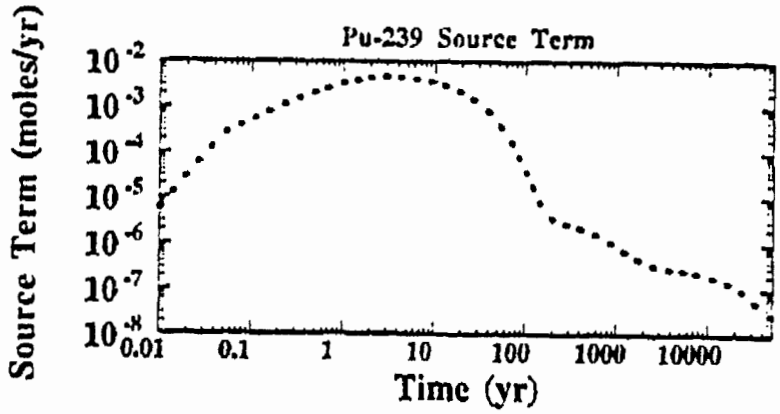

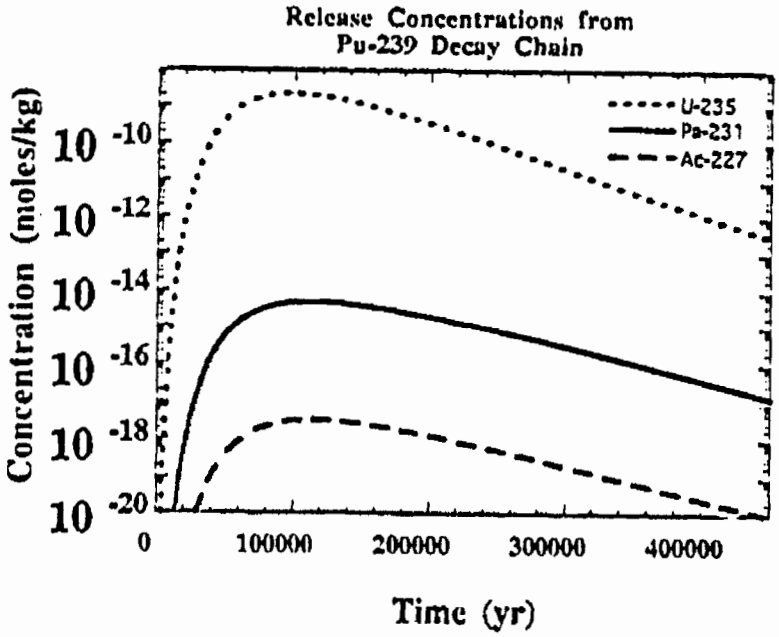

Figure 21. (a) Source term and (b) Concentration breakthrough curve for Pu-239.

Pu-240

The figures below show the time-dependent source term and concentration breakthrough curve for the Pu-240 decay chain: Pu-240 -> U-236 -> Th-232 -> Ra-228. Again, we estimate the arrival times of the peaks using the screening technique described above. We expect the Pu-240 peak to occur after about 4 million years. This time is much longer than its half-life of 6,570 years, and no release of Pu-240 occurs. The U-236 peak should occur at about 76,000 years based on its Kd of 1.8 and a lag time of 6000 years to account for some ingrowth of this species. The actual peak occurs at 81,950 years. The next two daughter products, Th-232 and Ra-226, have very flat breakthrough curves because their ingrowth depends on the long half-life of U-236, 7 x 10^8 years.

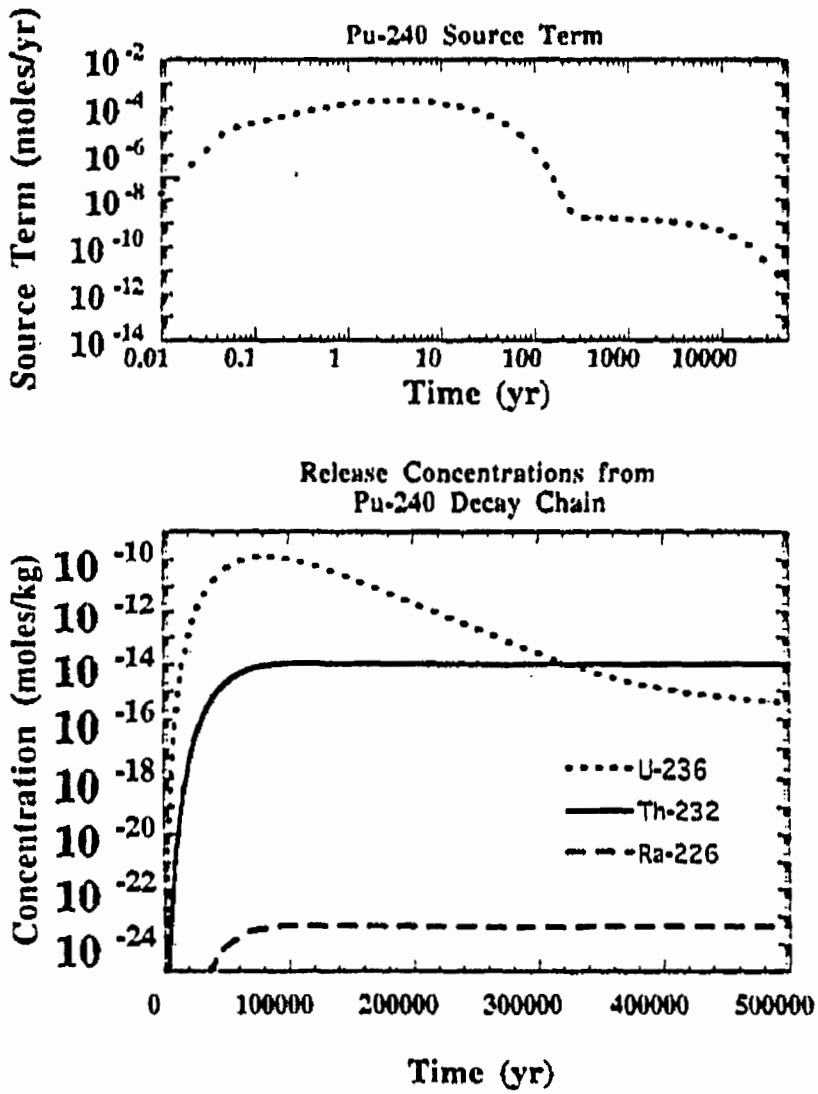

Figure 22. (a) Source term and (b) Concentration breakthrough curve for Pu-240.

Pu-241

The figures shown below give the source term and concentration breakthrough curve for the Pu-241 decay chain: Pu-241 -> Am-241 -> Np-237 -> U-233. In this case, neither the parent nor the first daughter, Am-241, breakthrough to the monitoring point because of their short half-lives, 14.4 years and 432 years, respectively. We expect to see the peak for the second daughter product, Np-237, after about 4,500 years with a lag on the order of 400 to 500 years to allow the first two species to decay. The peak occurs at 5,099 years. The U-233 occurs shortly after the Np-237 peak. Again, slow decay of Np-237 produces a relatively constant source term for the U-233 and the breakthrough curve has a flat tail over the 30,000-year time scale of this simulation.

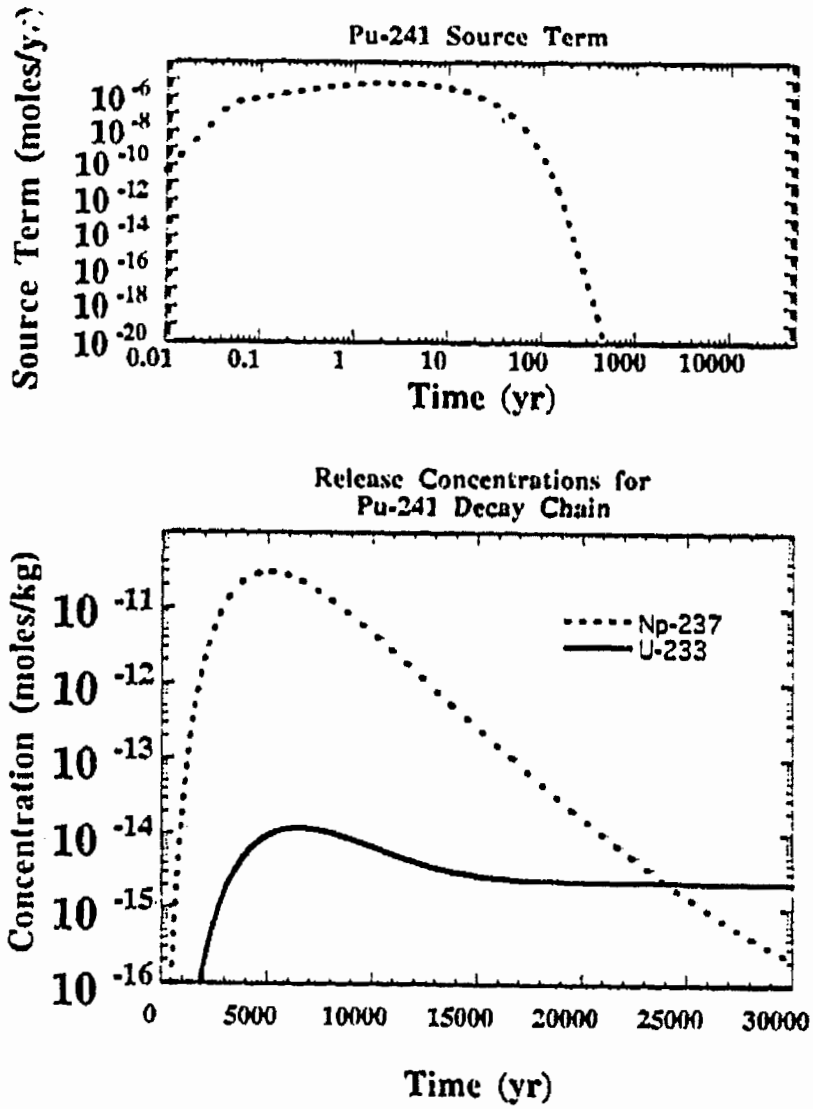

Figure 23. (a) Source term and (b) Concentration breakthrough curve for Pu-241.

Pu-242

The source term and concentration breakthrough curve for the Pu-242 decay chain are shown in the figures below. The decay chain for this species is : Pu-242 -> U-238. Pu-242 should peak after about 4 x 10^6 years. We don't run the simulation that long, but can see that the Pu-242 curve is still growing after two million years. The U-238 peak should take 70,000 years (based on its Kd) with a relatively long lag time for ingrowth because of the 376,000 year half-life of Pu-242. The actual peak occurs at 156,000 years but tapers off linearly because of the slow decay of Pu-242.

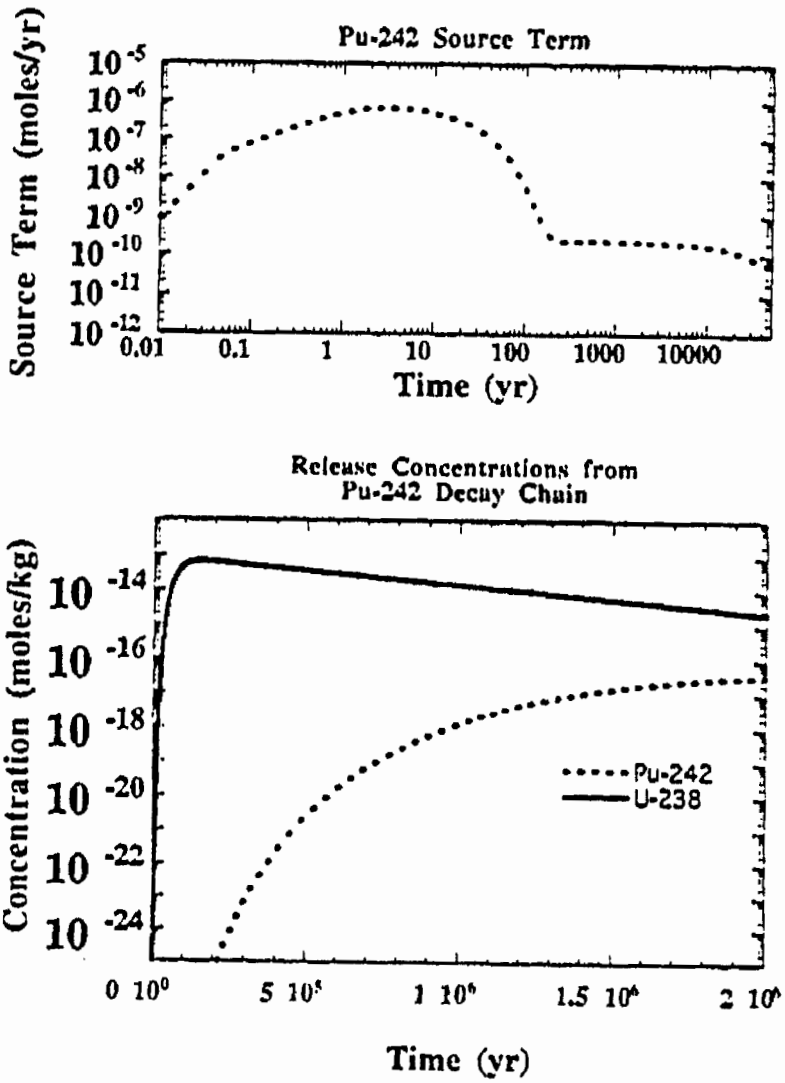

Figure 24. (a) Source term and (b) Concentration breakthrough curve for Pu-242.

Tc-99

The time-dependent source term and concentration breakthrough curve for Tc-99 follow. This species has no daughter products. The peak for this species occurs after 16,000 years as predicted using its sorption coefficient of 0.3.

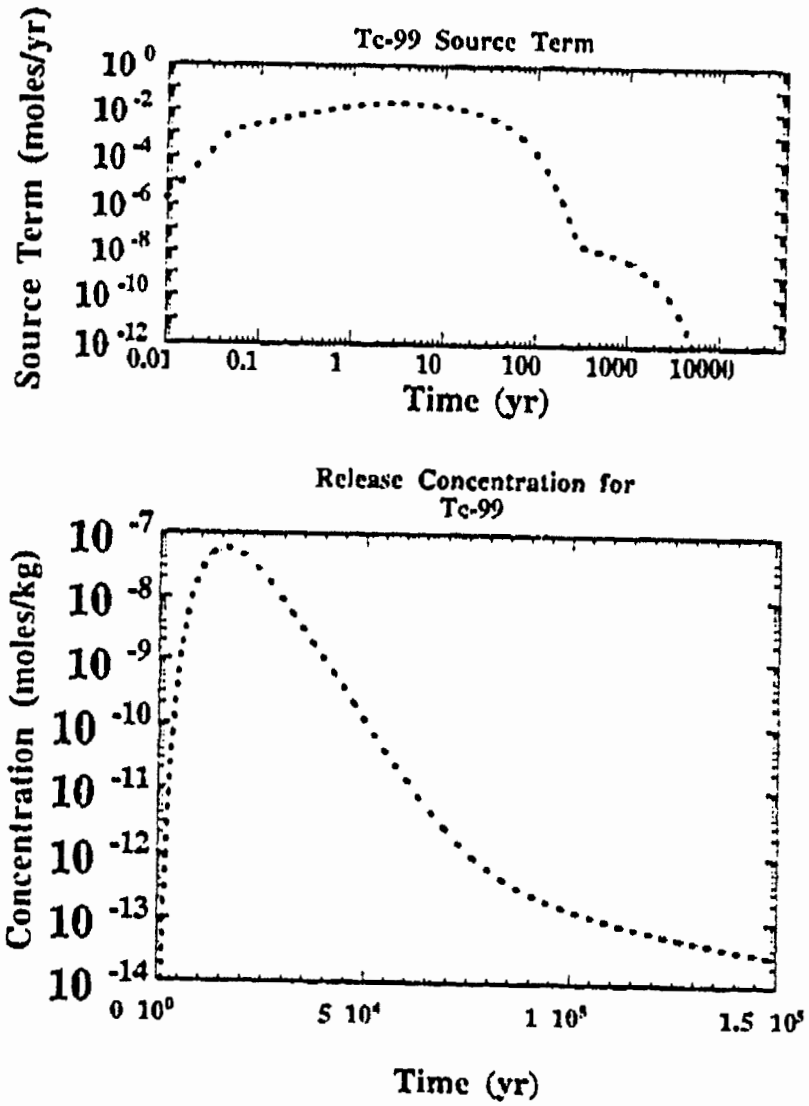

Figure 25. (a) Source term and (b) Concentration breakthrough curve for Tc-99.

Th-232

The figures below show the time-dependent source term and the concentration breakthrough curve for Th-232, which forms no daughter products. The source term for this species is constant for 8.5 x 10^7 years because its release is solubility limited. This produces a flat breakthrough curve similar to that seen for Hf-182.

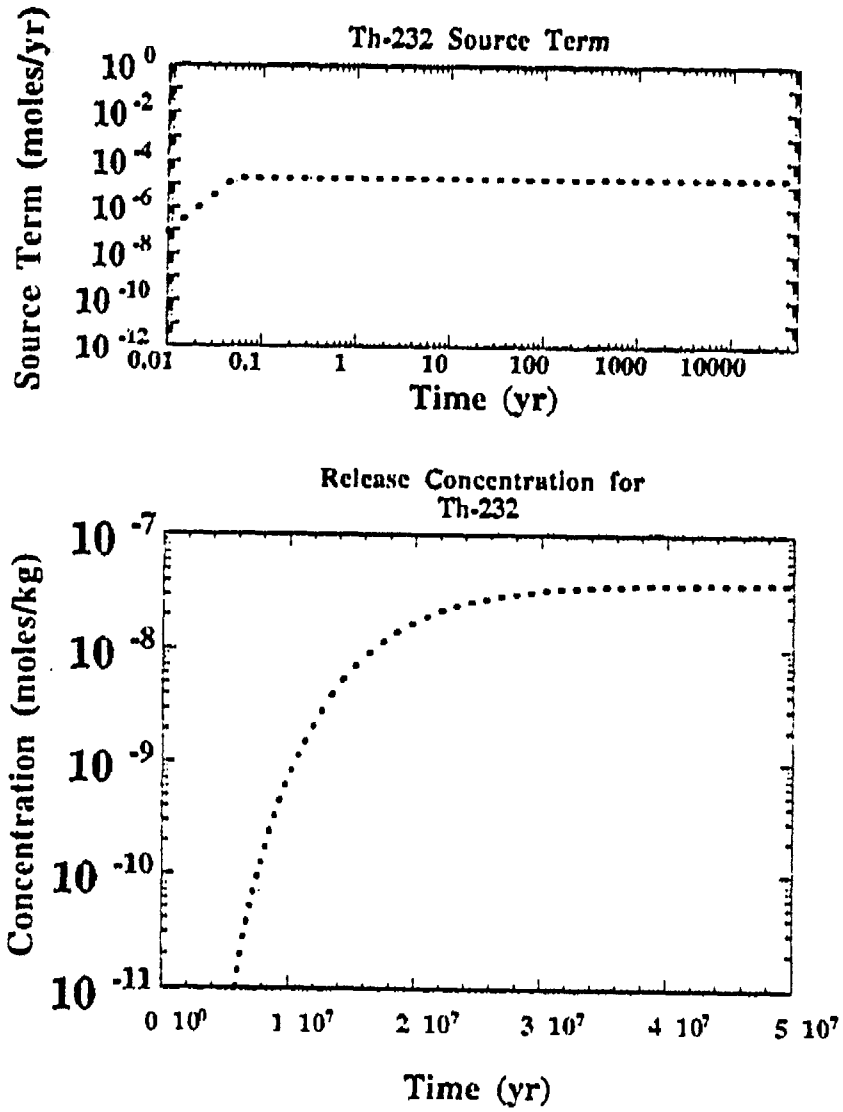

Figure 26. (a) Source term and (b) Concentration breakthrough curve for Th-232.

U-233

The time-dependent source term and concentration breakthrough curve for the U-233 decay chain are shown in the figures below. U-233 decays to form Th-229. We expect to see the U-233 peak after 70,000 years. It occurs at 71,950 indicating that the calculation is correct. The Th-229 peak occurs shortly after this. The Th-229 breakthrough curve ramps downward because its half-live is short, 7340 years, compared to its rate of formation (half-life for U-233 is 162,000 years) and to the simulation time.

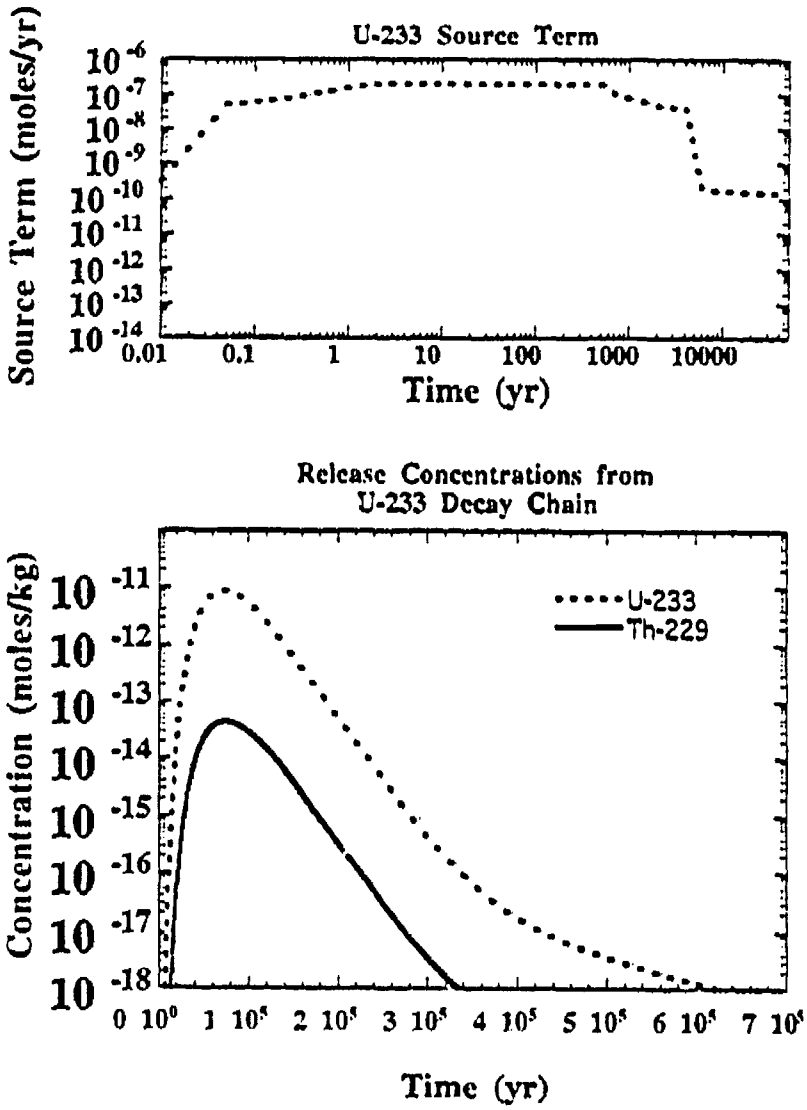

Figure 27. (a) Source term and (b) Concentration breakthrough curve for U-233.

U-234

The figures below show the time-dependent source term and concentration breakthrough curves for the U-234 decay chain: U-234 -> Th-230 -> Ra-226 -> Pb-210. We expect to see the U-234 peak after about 70,000 years, and it occurs at 74,480 years. These results are very similar to those for the Pu-238 chain because the chain is the same. The Th-230, Ra-226, and Pb-210 peaks occur shortly after the U-234 peak, and the tails on the breakthrough curves for these daughter products ramp downward in time.

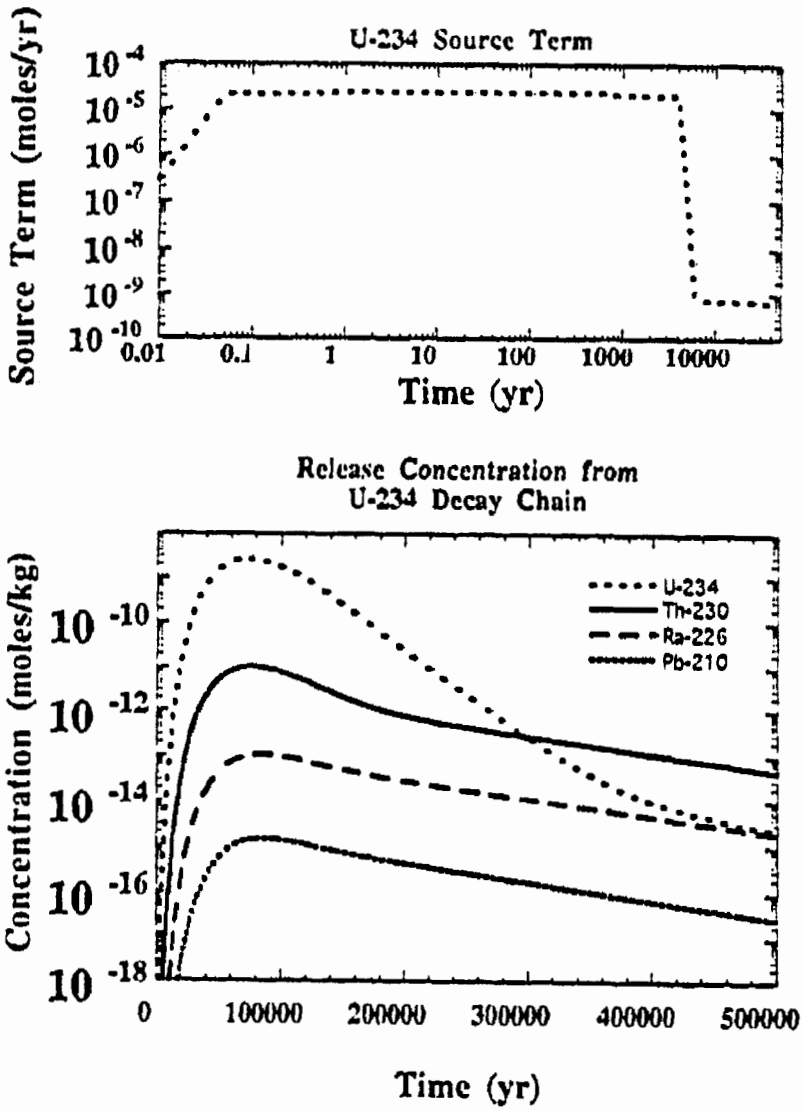

Figure 28. (a) Source term and (b) Concentration breakthrough curve for U-234.

U-235

The time-dependent source term and concentration breakthrough curve for the U-235 decay chain are shown below. U-235 decays to Pa-231. Again, we expect to see the Uranium peak after about 70,000 years. The peak occurs at 74,450. There is a very slight peak for the Pa-231 at about 100,000 years, but the tail for this species is flat because of very slow ingrowth.

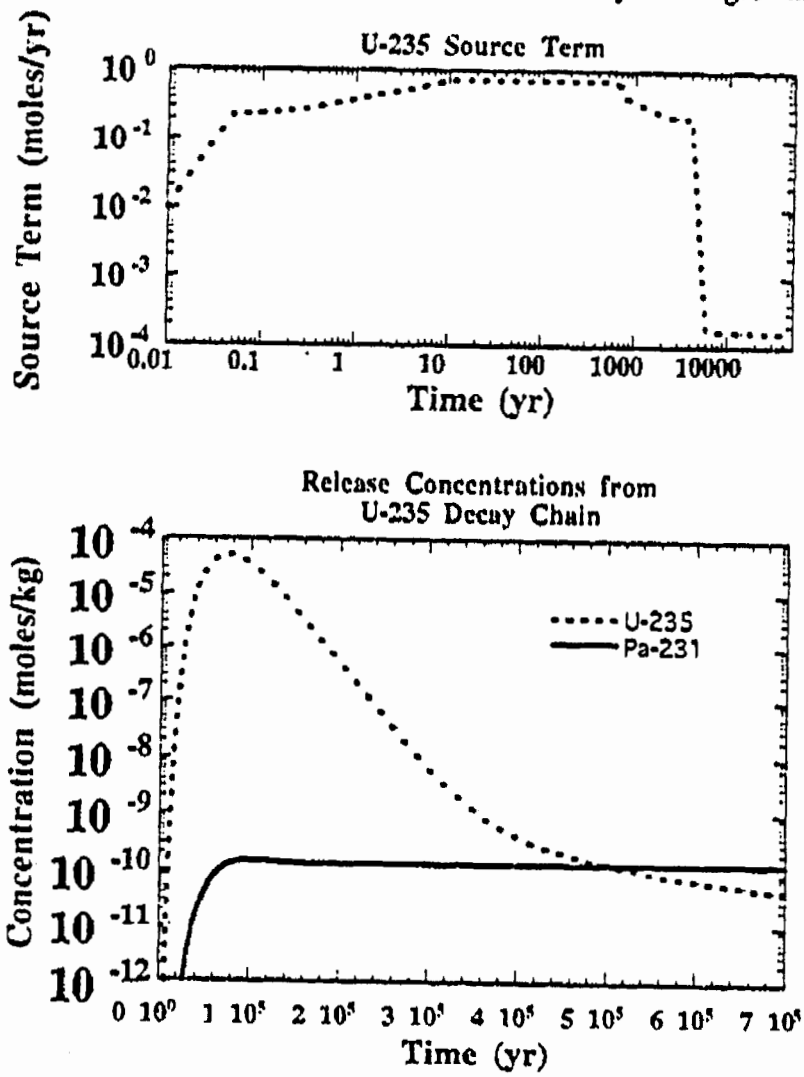

Figure 29. (a) Source term and (b) Concentration breakthrough curve for U-235.

U-236

The time-dependent source term and concentration breakthrough curve for U-236 are shown below. U-236 has no daughter products. Its peak concentration occurs after 75,110 years which again is quite close to the 70,000-year time estimated from the generic source term runs.

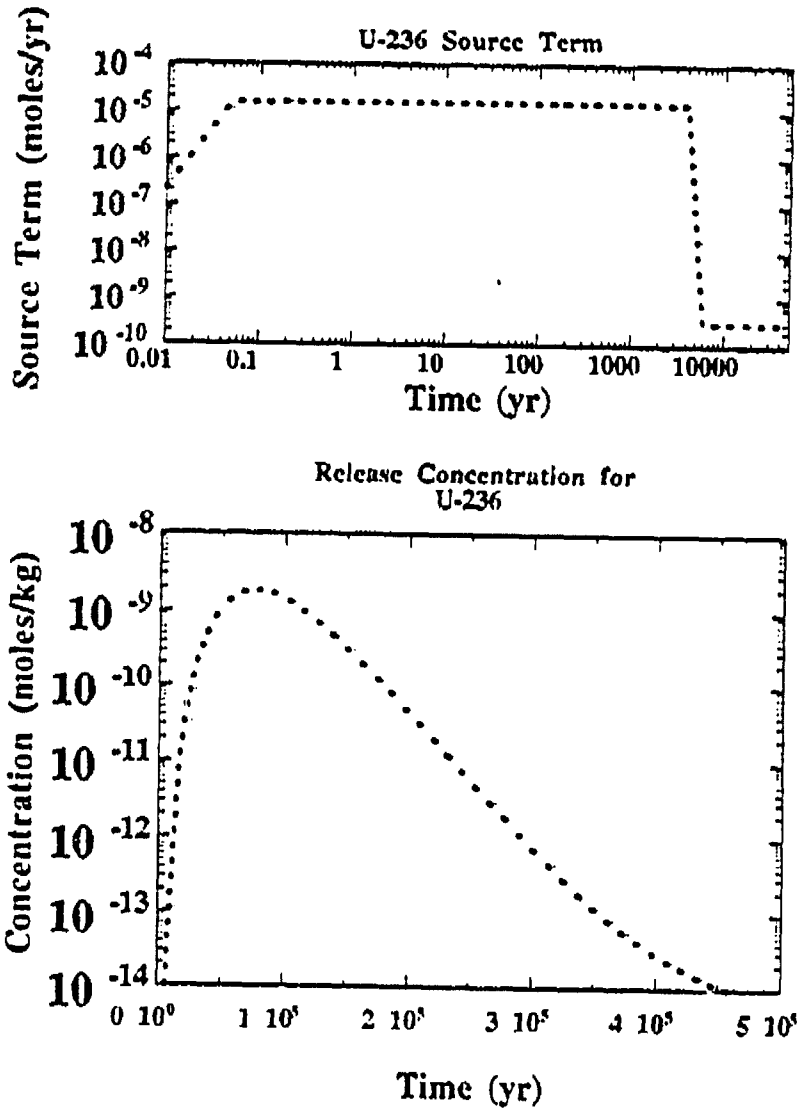

Figure 30. (a) Source term and (b) Concentration breakthrough curve for U-236.

U-238

The figures below show the source term and breakthrough curves for the U-238 decay chain: U-238 -> U-234 -> Th-230 -> Ra-226. The U-238 peak occurs at 74,950 years which is consistent with the rest of the Uranium calculations. The U-234, Th-230, and Ra-226 peaks occur shortly after this time, but with much lower concentrations because of the long half-life of U-238, 4.47 x 10^9 years.

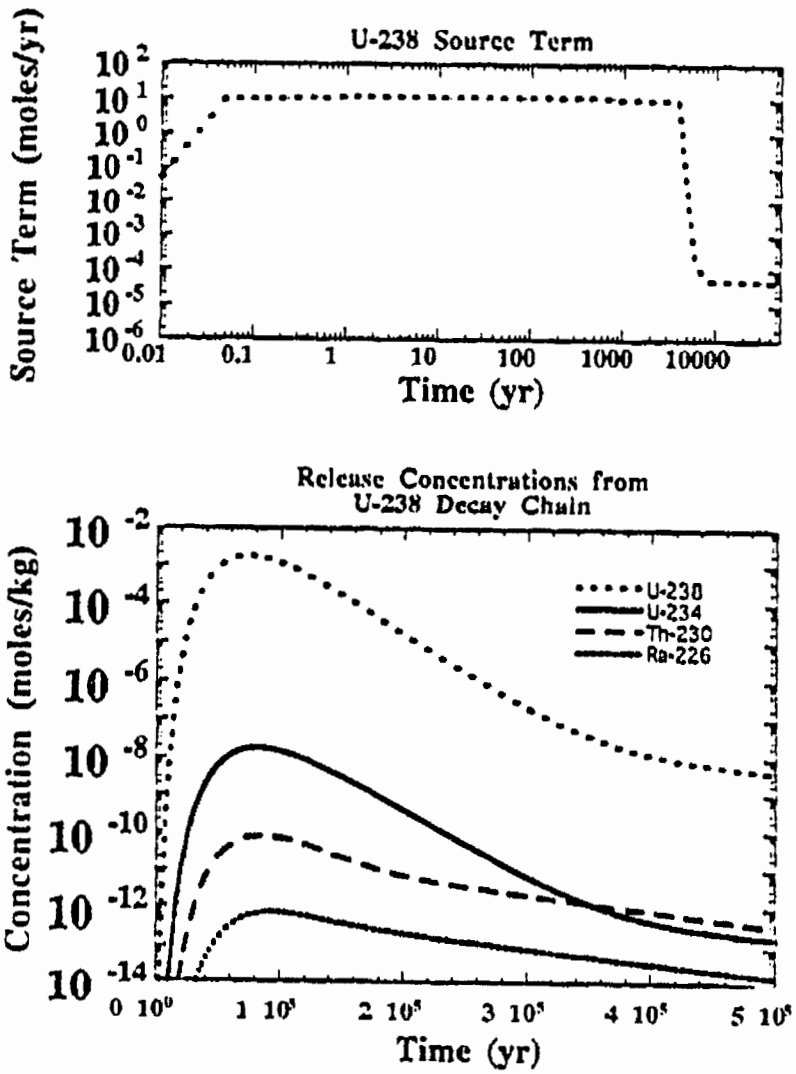

Figure 31. (a) Source term and (b) Concentration breakthrough curve for U-238.

Summary of Results

The results from these transport calculations are input to the aquifer dilution model (Vold, 1995) which in turn are used for human dose assessment calculations (Shuman, 1995). Release from the vadose-zone transport calculations enter into the dose predicted for the Postinstitutional control period, a period of 10,000 years after institutional control of the site has ended (DOE Order 5820.2A). The parent radionuclides Am-241, C-14, Pu-241, and Np-237 are considered to be the most important to the Performance Assessment of MDA G because these species reach their peak concentrations before 10,000 yrs. Np-237 is transported more quickly than most species because of its very low Kd (0.007) which leads to a peak concentration at 4500 yrs. Am-241 and Pu-241 both decay rather quickly to Np-237 which results in their relatively short travel times. C-14 does not sorb, and peaks at about 3,900 yrs. The water chemistry of C-14 is complex and leads to losses as CO_2 gas, but we treat it as a conservative water-phase tracer in this calculation.

The following parent nuclides require subsurface transport calculations, but reach peak concentrations at times greater than 10,000 yrs: Hf-182, Pu-238, Pu-239, Pu-240, Pu-242, Tc-99, Th-232, U-233, U-234, U-235, U-236, and U-238. The peak arrival time for those species requiring full transport calculations is shown in Table 6. Mo-93 shows no release to the basalts. The following nuclides were eliminated from further consideration because their half-lives are short compared to there transport rates: Ag-108m, Ba-133, Cd-113m, Co-60, Cs-137, Eu-152, Eu-154, Gd-148, H-3, Sm-151, Sr-90, Nb-94, and Ra-226.

Table 6. Peak Arrival Times for Nuclides requiring Full Transport Calculations

Radionuclide	Peak Arrival Time (yr)
Am-241	(no release)
Np-237	5,068
U-233	6,505
Th-229	7,779
C-14	3,890
Hf-182	(no peak)
Np-237	4,500
U-233	5,924
Th-229	7,217
Pu-238	(no release)
U-234	70,950
Th-230	73,950
Ra-226	80,540
Pb-210	82,450
Pu-239	(no release)
U-235	97,950
Pa-231	113,500
Ac-227	113,500

Pu-240	(no release)
U-236	81,950
Th-232	112,000
Ra-228	112,000
Pu-241	(no release)
Am-241	(no release)
Np-237	5,099
U-233	6,500
Pu-242	>2.0e6
U-238	156,000
Tc-99	16,000
Th-232	(no peak)
U-233	71,950
Th-229	73,950
U-234	74,480
Th-230	76,550
Ra-226	84,480
Pb-210	86,550
U-235	74,450
Pa-231	100,400
U-236	75,110
U-238	74,950
U-234	81,950
Th-230	85,450
Ra-226	92,950

The results from these transport calculations are input to the aquifer dilution model (Vold, 1995) which also requires a value for the vadose-zone darcy velocity. We reported a value of 2.59 mm/yr which corresponds to the velocity at the breakthrough monitoring point.

Many assumptions are implicit to these results and are discussed throughout the report. However, here we will point out assumptions that are thought to make the calculations conservative. The most conservative assumption is that the transport results assume that flow and transport through the lower three units (Guaje Pumice, Cerros del Rio basalts and the Puye Formation) are instantaneous. We take no account for these units because the data that exist are sparse and show high variability. This assumption is very conservative as these units account for approximately 70% of the unsaturated zone, as shown in Figure 1.

The concentrations reported represent both the earliest breakthrough and the highest concentrations reaching the top of the basalt. The monitoring point is located beneath a cluster of pits and also beneath the two pits that are the deepest and have the largest pits volumes, which results in a larger source term for these simulations. Also, this point is located within the basalt unit which has no sorption. The liquid concentration that is reported represents the full dose reaching that point.

DISCUSSION OF UNCERTAINTY

As in any predictions of long-term radionuclide migration through the subsurface, the results of these transport simulations inherently contain many uncertainties. Here we will assess what we think are the greatest uncertainties and discuss their impact on the results.

As discussed above, these results take no credit for transport times through the lower three hydrogeologic units because of a great uncertainty associated with the hydrologic data for these units. Because these units make up approximately 70% of the vadose zone, this assumption is extremely conservative. The inclusion of these units is likely to add several thousand to tens of thousands of years to transport times, and result in lower peak concentrations to the saturated zone. The dose assessment calculations show that releases due to vadose-zone transport contribute very little to the human dose calculated from the historic inventory located at MDA G (Shuman, 1995). An uncertainty that adds conservatism to the transport results probably doesn't warrant further study at this time. This issue may need to be revisited if releases by vadose-zone transport which include the Legacy Waste Inventory are more significant to the calculated human dose.

The steady flow assumption is an uncertainty that is related to an understanding of the processes that control flow at the site. The use of this assumption warrents further study because it is unclear whether its use leads to conservative or non-conservative results. The site conceptual model (Turin, 1995) describes the site as a transient system that alternates between an episodic infiltration state and a normal drying state. The transport simulations are based on a steady, background flow rate of 1 mm/yr that flows continuously from the top of the mesa through the underlying units. We feel that the hydrology of the mesa top units may be strongly controlled be evaporation. The low, steady infiltration rate indirectly accounts for evaporation by yielding low saturations. However, by explicity including evaporation in a transient fashion, we may see different results. It is possible that the mesa and the sub-units are not strongly connected hydrologic systems. The wetter saturations beneath the mesa may be the result of recharge from a different source than recharge through the mesa top. The mesa itself may act as a dry barrier to downward migration of waste which could lead to enhanced waste isolation.

The fracture infiltration study lead us to the conclusion that fracture flow is diffucult to initiate (e.g. requires a large source of water) and is short-lived once the water source is removed. This conclusion helps justify the use of the equivalent continuum model for the subsequent transport calculations. However, if some fractures do flow periodically, pulses moving through these fractures could potentially lead to faster transport of contaminants. In the fracture infiltration study, we considered only infiltration events. Another important consideration is the effect of the drying out period between infiltration events. The time between infiltration events that is necessary for evaporative conditions to effectively nullify the infiltration is unknown. Also the effect of these alternate periods of wetting and drying on contaminant transport down the fractures is unknown and warrents further study.

The steady pit infiltration rate is a further uncertainty contained in the transport simulations. The mean pit percolation rate of 4 mm/yr stems from a series of Monte Carlo simulations that yields a range in annual percolation from 0.0 mm to 120 mm. The distribution is highly skewed toward the low end with 80% of the values equal to 0.0 mm (Springer, 1995). We plan to address the uncertainty associated with using a steady pit infiltration rate by running a few transient runs with variable annual pit percolation rates to determine whether transient pit infiltration averages to some steady value. Similar studies that consider the background infiltration rate may also be considered.

As shown in Figure 15, the transport simulations are very sensitive to the value of the sorption coefficient, Kd. Uncertainty in this parameter for weakly sorbing nuclides is a data uncertainty that can play an important role in the results of the transport simulations and the subsequent human dose assessment calculations. From Table 2, we see that nuclides having a Kd value of 1.0 or less, first arrive at the basalts in a period of 10,000 years or less. A lower Kd for some of the more prevalent nuclides (e.g., uranium) could lead to much higher doses. The Kd values that are used in this PA (Krier, et al, 1995) are based on values measured for Yucca Mountain tuffs. Site

specific values for nuclides which are weak sorbers or have large source terms should help decrease the uncertainty in the transport calculations that results from the data uncertainty in this property.

At this point, we feel that uncertainty associated with the hydrologic processes themselves (conceptual model uncertainty) dominates our ability to make predictions of transport at the site more so than uncertainty associated with the hydrologic and geochemical properties (data uncertainty).

REFERENCES

Bowen, B.M., "Los Alamos Climatology, "Los Alamos National Laboratory Report LA-11735-MS, 1990.

Barnard, R.W. and H.A. Dockery, "Technical Summary of the Performance Assessment Calculation Exercises for 1990 (PACE90)," Sandia National Laboratories Report SAND 90-2726, 1991.

Hollis, D., E. Vold, K. Birdsell, H.J. Turin, P. Longmire, E. Springer, W. Hansen, D. Krier, R. Shuman, "Performance Assessment of LANL TA-54, Area G, Low-Level Radioactive Waste Disposal Facility," Los Alamos National Laboratory Draft Document: August 6, 1995.

Krier, Donathon, Patrick Longmire, and H. J. Turin, "Geologic, Geohydrologic and Geochemical Data Summary of MDA G, TA-54, Los Alamos National Laboratory", Los Alamos National Laboratory Report LA-UR-95-2696, 1995.

Nilson, R.H., E.W. Peterson, K.H. Lie, N.R. Burkhard, and J.R. Hearst, "Atmospheric Pumping: A Mechanism Causing Vertical Transport of Contaminated Gases Through Fractured Permeable Media", J. of Geophysical Research, Vol. 96, B13, pp. 21933-21948, 1991.

Nitao, J.J., Theory of Matrix and Fracture Flow Regimes in Unsaturated, Fractured Porous Media, in High Level Radioactive Waste Management, Proc. of the 4th Annual Int'l Conf., Las Vegas, NV:845-852, 1991.

Purtyman, W.D., "Hydrologic Characteristics of the Main Aquifer in the Los Alamos Area: Development of Ground Water Supplies", Los Alamos National Laboratory Report LA-9957-MS, 1984.

Rogers, D.B., E.L. Vold, and B. M Gallaher, "Bandelier Tuff Hydraulic Characteristics from Los Alamos National Laboratory Borehole G-5 at MDA G, TA-54", Los Alamos National Laboratory report, LA-UR-95-3129, 1995.

Rosenberg, N.D., W.E. Soll, and H.J. Turin, "Potential Transport of PCBs Through Fractured Tuff at Area G", Los Alamos National Laboratory report LA-UR-94-28, 1993.

Rosenberg, N.D. and H.J. Turin, "Summary of Area G Geology, Hydrogeology, and Seismicity for Radiological Performance Assessment", Los Alamos National Laboratoy report LA-UR-93-3081, 1993.

Turin, H. J., "Subsurface Transort Beneath MDA G: A Conceptual Model", Los Alamos National Laboratory report LA-UR 95-1663, 1995.

Soll, W.E., "Influence of Fracture Fills and Fracture Coatings on Flow in Bandelier Tuff", Los Alamos National Laboratory report LA-UR-95-2695, 1995.

Shuman, R., "Dose Assessment Methodology For Offsite Individuals and Inadvertent Intruders" Performance Assessment of LANL TA-54, Area G, Low-Level Radioactive Waste Disposal Facility, Appendix 3K, Los Alamos National Laboratory Draft Document: August 6, 1995.

Springer, E. P., "Area G Performance Assessment: Surface Water and Erosion", Los Alamos National Laboratory report LA-UR-95-2497, 1995.

van Genuchten, M.A., Closed-Form Equation for Predicting the Hydraulic Conductivity of Unsaturated Soils. SSSA J, 44 :892-898, 1980.

Vold, Erik, "A Liquid Phase Source Release Model with Application to the LANL LLRW Disposal Site Performance Assessment", Area G, Low-Level Radioactive Waste Disposal Facility, Appendix 3B, Los Alamos National Laboratory Draft Document: August 6, 1995.

Vold, Erik, "Atmospheric Transport in Complex Terrain", Performance Assessment of LANL TA-54, Area G, Low-Level Radioactive Waste Disposal Facility, Appendix 3J, Los Alamos National Laboratory Draft Document: August 6, 1995.

Vold Erik, "Aquifer Dilution Model", Performance Assessment of LANL TA-54, Area G, Low-Level Radioactive Waste Disposal Facility, Appendix 3I, Los Alamos National Laboratory Draft Document: August 6, 1995.

Weeks, E.P., "Effect of Topography on Gas Flow in Unsaturated Fractured Rock", Flow and Transport Through Unsaturated Fractured Rock, AGU Geophysical Monograph #42, pp. 165-170, 1987.

Wood, M.I., R. Khaleel, P.D. Rittmann, A.H. Lu, S.H. Finfrock, R.J. Serne, K.J. Cantrell, T.H. DeLorenzo, "Performance Assessment for the Disposal of Low-Level Waste in the 200 West Area Burial Grounds," Westinghouse Hanford Company report WHC-EP-0645, 1994.

Zyvoloski, G. A., B. A. Robinson, Z. V. Dash, and L. L. Trease, "Models and Methods Summary for the FEHMN Application", Los Alamos National Laboratory report LA-UR-94-3787, Rev. 1, 1995.

Zyvoloski, G. A., B. A. Robinson, Z. V. Dash, and L. L. Trease, "User's Manual for the FEHMN Application", Los Alamos National Laboratory report LA-UR-94-3788, Rev. 1, 1995.